NEUROPHOTONICS

RESEARCH PAPER

Toward a brighter constellation: multiorgan neuroimaging of neural and vascular dynamics in the spinal cord and brain

Dmitrijs Celinskis,[a] Christopher J. Black,[a] Jeremy Murphy,[a] Adriel Barrios-Anderson,[a] Nina G. Friedman,[a] Nathan C. Shaner,[b] Carl Y. Saab,[c] Manuel Gomez-Ramirez,[d] David A. Borton,[a,e,f,*] and Christopher I. Moore[a,*]

[a]Carney Institute for Brain Science, Providence, Rhode Island, United States
[b]University of California San Diego, School of Medicine, La Jolla, California, United States
[c]Cleveland Clinic Lerner Research Institute, Neurological Institute, Department of Biomedical Engineering, Cleveland, Ohio, United States
[d]University of Rochester, School of Arts and Sciences, Rochester, New York, United States
[e]Brown University, School of Engineering, Providence, Rhode Island, United States
[f]Center for Neurorestoration and Neurotechnology, Providence VA Medical Center, Providence, Rhode Island, United States

ABSTRACT. **Significance:** Pain comprises a complex interaction between motor action and somatosensation that is dependent on dynamic interactions between the brain and spinal cord. This makes understanding pain particularly challenging as it involves rich interactions between many circuits (e.g., neural and vascular) and signaling cascades throughout the body. As such, experimentation on a single region may lead to an incomplete and potentially incorrect understanding of crucial underlying mechanisms.

Aim: We aimed to develop and validate tools to enable detailed and extended observation of neural and vascular activity in the brain and spinal cord. The first key set of innovations was targeted to developing novel imaging hardware that addresses the many challenges of multisite imaging. The second key set of innovations was targeted to enabling bioluminescent (BL) imaging, as this approach can address limitations of fluorescent microscopy including photobleaching, phototoxicity, and decreased resolution due to scattering of excitation signals.

Approach: We designed 3D-printed brain and spinal cord implants to enable effective surgical implantations and optical access with wearable miniscopes or an open window (e.g., for one- or two-photon microscopy or optogenetic stimulation). We also tested the viability for BL imaging and developed a novel modified miniscope optimized for these signals (BLmini).

Results: We describe "universal" implants for acute and chronic simultaneous brain–spinal cord imaging and optical stimulation. We further describe successful imaging of BL signals in both foci and a new miniscope, the "BLmini," which has reduced weight, cost, and form-factor relative to standard wearable miniscopes.

Conclusions: The combination of 3D-printed implants, advanced imaging tools, and bioluminescence imaging techniques offers a coalition of methods for understanding spinal cord–brain interactions. Our work has the potential for use in future research into neuropathic pain and other sensory disorders and motor behavior.

 [DOI: 10.1117/1.NPh.11.2.024209]

*Address all correspondence to Christopher I. Moore, christopher_moore@brown.edu; David A. Borton, david_borton@brown.edu

Keywords: brain; spinal cord; bioluminescence; multiorgan imaging; fluorescence; implantable window; miniscope; two-photon; sensory processing

Paper 23124SSR received Dec. 5, 2023; revised Mar. 18, 2024; accepted Mar. 19, 2024; published May 7, 2024.

1 Introduction

Emergent biological phenomena, such as mammalian behavior, inherently depend on multiple computations conducted by distinct subsystems and the real-time interactions between them. Although iterative study of subsystems in isolation can be highly beneficial, conjoint dynamics across systems, which could reflect distributed shared computations or essential interactive updating of distinct computations, are also essential to comprehending system function. As such, understanding these complex interdependencies also requires simultaneously recording biological activity across multiple organs.

Pain is a canonical example of a complex emergent phenomenon dependent on multiple subsystems. This clinically essential problem is still insufficiently understood and addressed. Painful sensations evolved from nociceptive signaling of peripheral etiology and implicated a wide array of chemical interactions and cell types (Fig. 1 lists a subset of implicated signals). These signals navigate from skin to spinal cord and ascend to the brain. Although this classic "feedforward" pathway description is intuitive, re-entrant feedback loops exist at all levels that impact pain sensation, including local reflex loops,[1,2] descending projections,[3] and motor behavioral modification.[1,4,5]

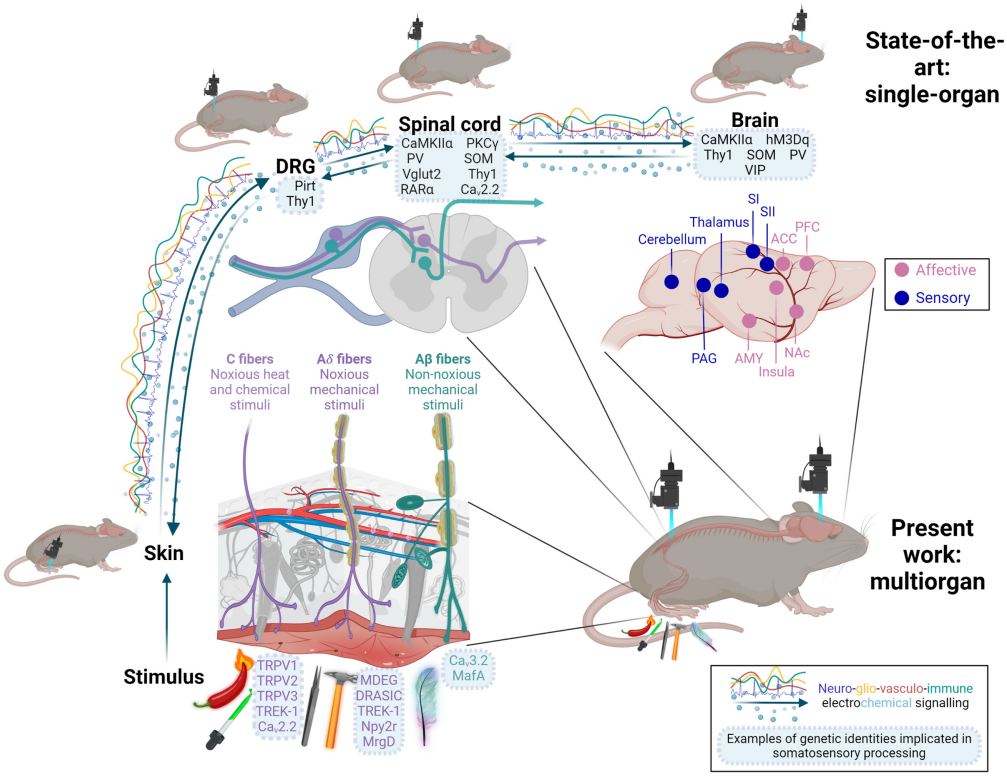

Fig. 1 A key use case for multiorgan imaging: studying mechanisms of nociception and pain peripheral nociceptive input that drives pain engages a wide range of dynamic body systems. Integrated activity spans multiple organs, including skin, dorsal root ganglia, spinal cord, and brain, and depends critically on a broad array of networks, including neural, vascular and immune signaling. State-of-the-art approaches for studying sensory information processing typically rely on *in vivo* imaging in one organ and focuses on neurons. In this work, we expand the *in vivo* methodological toolbox by developing procedures for multiorgan *in vivo* studies. This figure was created fully with BioRender, Ref. 74.

Direct imaging of activity and structure provides a powerful approach to capture the activity of specific cell types and is typically essential to observe dynamics in the many nonneural systems that help create behavior and perceptual phenomena, such as pain.[6] Using genetically targeted fluorescent (FL) indicators, typical imaging studies target a single body area,[7–9] including the brain,[7] spinal cord,[8,10] dorsal root ganglion,[11] skin,[12,13] heart,[14] or intestinal tissue.[15] Single area approaches necessitate using independent animals to study each site and miss the potentially crucial interdependence between different body parts in generating phenomena. Further, this approach also leads to an increased number of animals needed for studies, leading to greater costs and unexplained experimental variability. Imaging methods, such as functional magnetic resonance imaging (fMRI), that provide whole-brain and spinal cord access with the ability to resolve and stimulate single brain regions[16,17] and brain–spinal cord at the same time[18] have been transformative to our understanding of multisubsystem interdependencies in behavior. However, fMRI lacks the single-neuron resolution, temporal precision, and genetic specificity possible with optical approaches.

Although all these factors suggest the need for multiorgan optical access with single-cell precision, there are several challenges to achieve this goal in mice. A significant hurdle to making multiorgan microscopy standard in live animals is the increased surgical complexity. Implantation of cranial and vertebral implants is typically done under anesthesia, and combining both procedures in a single animal can require longer loss of consciousness and increased risk of anesthetic exposure. As one example, isoflurane, in standard use for such implantations, shows cumulative effects of exposure[19] and can impact microstructural organization[20] and protein phosphorylation in the brain,[21] cause postoperative cognitive dysfunction,[22] increase susceptibility to anxiety-like behaviors,[23] and modulate cardiovascular function.[24] Importantly, exposure to isoflurane has also been reported to affect calcium dynamics in the spinal cord,[8] stimulate peripheral sensory nerves by sensitizing transient receptor potential V1 (Trpv1) receptors,[25] inhibit neuronal CaV3.2 calcium channels,[26] and increase the susceptibility to chronic pain by causing alterations in dorsal spinal cord and dorsal root ganglion.[27] Given these basic challenges, a key requirement for multisite imaging is the design of surgical procedures that minimize duration and that allow awake imaging if possible.

Further, the ability of animals to tolerate multiple window implants while maintaining health is also an open question. In addition to the potential immunological load created by multiple implants, they also create unique mechanical challenges, including steric hindrance between sites, and up to a doubling in the weight the animal must tolerate. In a small creature, such as a mouse, miniaturization of head implants needs to fall under ~ 2 g to avoid impeding behavior and normal motor function.[28] Also brain and spinal cord surgeries in mice require fine motor dexterity and nuanced microsurgical skills. Hence, availability of the neurosurgery personnel, ability to invest time into learning new surgical procedures and optimizing surgical training protocols to reduce training animal use are additional important considerations when implementing a novel surgical procedure as we present in this report.

FL imaging has been a remarkable, high-signal approach for tracking neural activity during behavior.[29–31] However, FL imaging is limited by its relatively high noise, created by factors such as tissue autofluorescence.[32,33] Dependence on excitation light also adds noise to small-target imaging in turbid media, as photons sent into tissue to elicit an FL scatter on the inbound path, creating image blurring and constraining imaging depth (Fig. 2). Furthermore, continuous application of external light, as typically employed with miniature microscopes ("miniscope") imaging, causes photobleaching,[41] phototoxicity,[42] and can adversely affect cellular capacitance[42,43] and mitochondrial function.[44] Additionally, FL miniscopes have been a great addition to the armamentarium of new tools for studying brain activity,[45–49] benefitting from low weight (2 g)[50] and effective optics. However, using this new gold standard for multisite imaging is a challenge, given the cumulative weight of multiple scopes, and this size issue grows with the need to increase simultaneously imaged colors or transition to wire-free scopes.

These issues with FL imaging may be addressed with bioluminescent (BL) indicators. BL indicators can provide robust calcium signals with relatively high spatiotemporal resolution.[51–55] Because BL signal production depends on a chemical interaction at the site of the indicator and not incoming light, it removes the need for excitation light. The noise due to scattering is essentially reduced by 50% (Fig. 2), photodamage is removed almost entirely as a concern, and

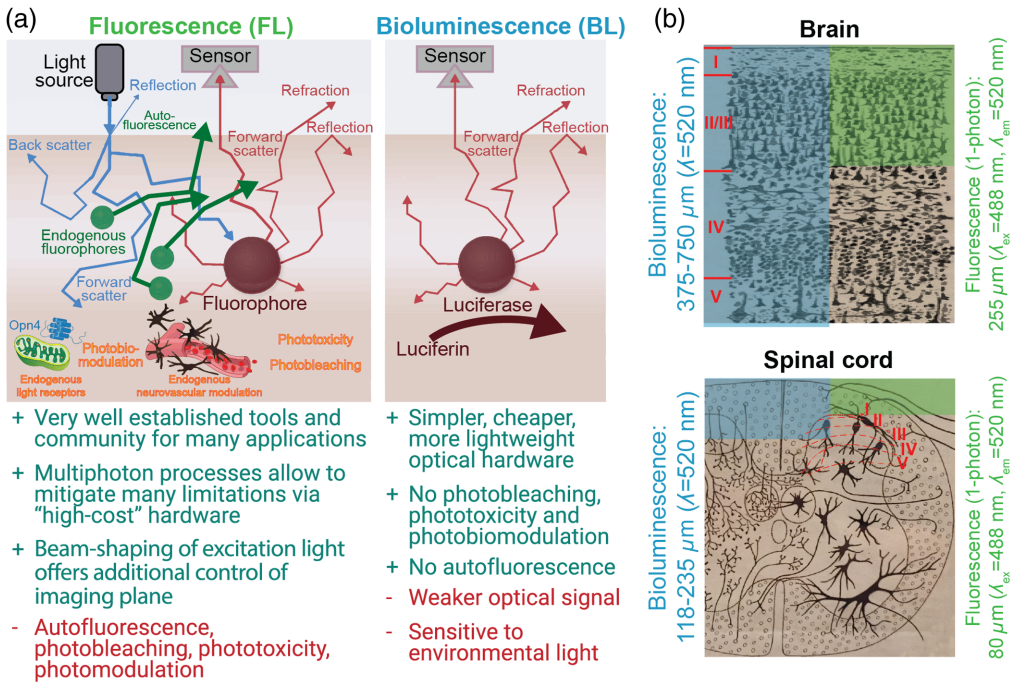

Fig. 2 Imaging BL offers advantages over FL, including decreased scattering artifacts and simplified optics (a) comparative advantages of BL and FL imaging. (b) BL offers up to 3× potential increase in imaging depth of discrete emitters (e.g., cells) compared to FL. Mouse somatosensory cortical layers and spinal dorsal horn laminae marked in red indicate the approximate deepest cortical layers[34–36] and laminae[35,37] that can be imaged in an adult mouse via one-photon FL and BL approaches. Imaging depths were determined from Ref. 38. The estimated increase in imaging depth is especially beneficial for spinal cord imaging because it is significantly constrained by photon scattering properties of myelin. The brain background image in (b) is from Ref. 39 and is in the public domain, the spinal cord image in (b) is from Ref. 40, licensed under Public Domain Mark 1.0. This figure was modified with permission from Ref. 59.

the removal of the excitation light further reduces the overall device weight. Further, for studies of multisite interactions during behavior, distinct BL indicators (e.g., emitting different colored signals) can be targeted to different subsystems throughout the body and monitored without the need for implants.

Here we took several steps toward a complete system for imaging neural and vascular dynamics in the brain and spinal cord with cellular resolution within the same mouse. We have developed custom implants that simplify and make brain–spinal cord procedures more accessible by reducing implant cost and fabrication complexity and by streamlining customization through 3D-printing. Our custom implant offers more versatility compared to prior implants, adapting to a wider range of use cases: brain or spinal cord, restrained or free behavior, wearable one-photon or benchtop 1 and two-photon imaging, and acute or chronic imaging for up to 230 days post-surgery. We show how to (i) fabricate versatile brain–spinal cord window implants, (ii) perform surgeries for brain and spinal cord within the same animal, (iii) habituate multi-implant animals for behavior, (iv) image anesthetized and awake animals simultaneously or sequentially across the brain–spinal cord, and (v) optically and mechanically modulate activity across these areas.

We take several steps to enable BL imaging that can overcome key constraints. We demonstrate that robust BL signals can be imaged in the brain. Further, we refined the design of UCLA miniscopes to improve signal sensitivity, reduce miniscope's weight, and simplify the assembly of hardware.

2 Materials and Methods

2.1 Animal Subjects

All procedures were approved by the Institutional Animal Care and Use Committee at Brown University. Mouse strains used in this study were purchased from Jackson Laboratory and

bred in-house: C57BL/6 wild-type mice, SOMcre x tdTomato x Ai148 (TIGRE-Ins-TRE2-LSL-GCaMP6f; JAX No. 030328), Trpv1$^{Chr2EYFP+/-}$ (Trpv1$^{Cre+/+}$ is JAX No.: 017769 and lox-STOP-lox-ChR2-EYFP is JAX No.: 012569), and Cacna1h$^{Chr2EYFP+/-}$. (Cacna1h$^{Chr2EYFP+/-}$ line were developed in the Lipscombe laboratory by mating Cacna1h$^{Cre+/+}$ with ChR2-EYFP$^{+/+}$, Cacna1h$^{Cre+/+}$ is also known as CaV3.2$^{Cre+/+}$; the Cacna1h$^{Cre+/+}$ mice used for this project were inbred 13 times). Mice were group-housed until the implant surgery and individually housed after the surgery. Mice were provided with bedding and nesting materials and maintained on a 12 h light–dark cycle in a temperature and humidity controlled environment.

2.2 Implant Fabrication

For ease of reference, we refer to our universal format 3D-printed implant as the UPRIM. All the implants tested for this work were 3D-printed via stereolithography. The 3D-printing photopolymer resins tested in this work included: (i) Accura Xtreme White 200, (ii) Accura SL 7820 in black color, (iii) Accura Xtreme in gray color, (iv) Accura 60, (v) Accura ClearVue, (vi) Dental SG (Formlabs, FLDGOR01), and (vii) Tough 1500_v1 (Formlabs, FLTO1501). We found both Dental SG and Tough 1500_v1 to be well suited for fabricating the spinal bars and implant chambers (Fig. 3). Dental SG offers better biocompatibility than Tough 1500_v1. However, based on the qualitative observations, we did not observe any differences between the two implants from these resins in terms of postsurgical animal behavior and tissue quality around the implant. The important considerations to keep in mind is the relatively high translucency and brittleness of the implants made from Dental SG resin. Transparency can be important in the optogenetic studies where it might be undesirable to confound the experimental results because of the endogenous effects resulting from the light exposure outside of the implanted window. Brittleness in our hands was a concern only when trying to thread the implant chamber directly. In contrast with the Tough 1500_v1, direct threading of Dental SG implants did not allow >1 screw–unscrew operation cycle. However, the issue of translucency can be addressed by painting the implant and the issue of brittleness can be resolved by gluing the commercially available nuts

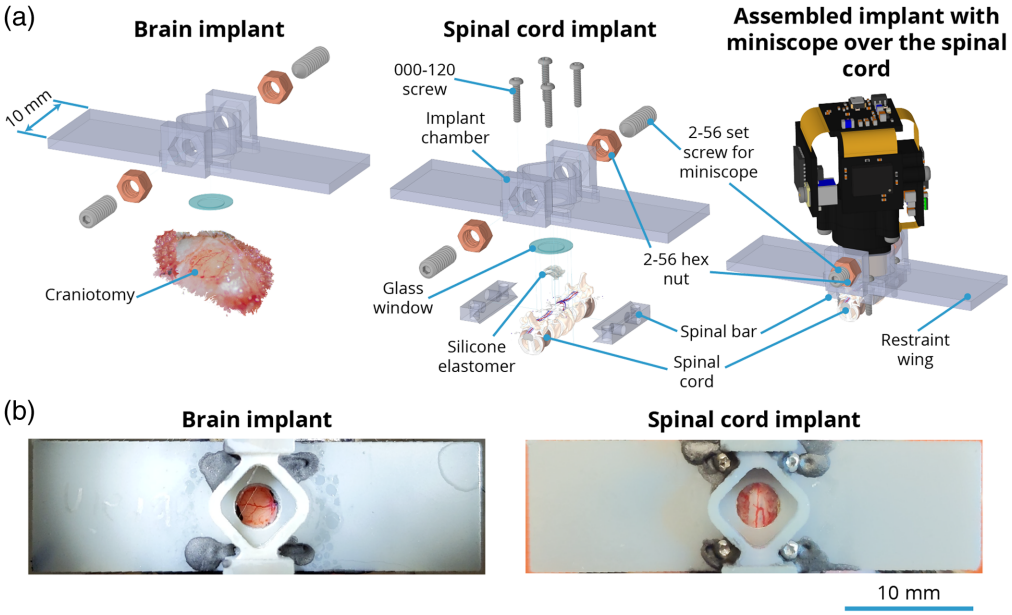

Fig. 3 UPRIM brain and spinal window implants consist of off-the-shelf components and a 3D-printed implant chamber. (a) Identical UPRIM implant chambers can be used for brain and spinal imaging. The only material difference is the need for additional parts to attach 3D-printed chamber to the spinal cord. The specific design illustrated here is equipped with a mount for UCLA miniscope v4, but can also be readily adapted for any wearable microscope and is compatible with the benchtop microscopes with ≥5 mm objective working distance. (b) Photos of the UPRIM 3D-printed implant chronically attached to the brain and the spinal cord.

into the implant. All the results presented in this report were collected using UPRIMs fabricated from Tough 1500_v1 resin (Fig. 3).

The spinal cord bars and spinal cord chamber were fabricated from Tough 1500_v1 resin using an in-house 3D-printer (Form 3, early 2019 edition, FormLabs Inc.). The fabrication steps were as follows:

(1) 3D-print the parts,
(2) wash parts in isopropyl alcohol (by hand or using Form Wash washer from FormLabs Inc.),
(3) perform only for the implant chamber: apply the UV-curing glue (electronic adhesive 123SBLUE, Norland Products Inc.) and insert the nuts (92736A101, McMaster-CARR Inc.),
(4) cure (using Form Cure, FormLabs Inc.),
(5) perform only for the implant chamber: after curing we usually apply additional small droplets of 5-min epoxy (QUIK-CURE, bSi Inc.) at the interface between the nuts and the implant,
(6) remove the supports,
(7) sand off any residual marks left while removing the supports,
(8) thread and test the fitting of all the cylindrical holes:
    (a) spinal cord bars:
        (i) hand-drill the cavities for the bar holders and make sure they fit well on the surgical bar holders;
        (ii) manually tap the vertical holes and test the fitting of the 000-120 screws (90910A603, McMaster-CARR Inc.);
    (b) implant chamber:
    (c) test the fitting of the 2-56 ¼″ set screws (90778A022, McMaster-CARR Inc.) into the glued nuts;
    (d) test the smoothness of the passage of 000-120 screws through the lateral vertical cavities used for threading the screws through the chamber into the spinal cord bars;
    (e) test the fit of the miniscope into the implant chamber;
(9) autoclave before the surgery.

At the time of writing, outsourced high-resolution stereolithographic 3D-printing from Accura 60 resin with quick clean finish is ~$76/implant (e.g., Ref. 56), and 3D-printing cost becomes negligible if using in-house 3D-printing. In contrast, spinal cord implants machined from stainless steel cost on the order of $349/implant for the individual implants or $171/implant when ordering in bulk (Neurotar Inc.). Further, our implant chambers are the first that allow imaging both in freely behaving animals with miniscopes and under restraint. Commonly available miniscope baseplates cost ≥$32/implant,[57] but they do not allow animal restraint and cannot be used for chronic spinal cord imaging.

2.3 Surgical Procedures

2.3.1 *Surgeries for brain AAV injections and window headpost implantation*

We performed brain injections of adeno-associated virus (AAV) and window headpost implantations as parts of a single procedure. Depending on the specifics of AAV injections, this surgical procedure takes on average 3 to 4 h plus 1 to 2 h of preparation time. All surgeries followed the aseptic techniques. We anesthetize mice using 1.5% to 2% isoflurane delivered in 100% oxygen gas and eliminated using vacuum suction. We protect the animal's eyes with sterile ocular ointment and maintain the animal's body temperature stable using a heating blanket. We prepare the surgical site on the skin in a dedicated area away from the surgical sterile field. We inject the animal with intraperitoneal (IP) dexamethasone (0.2 μg/g), subcutaneous (SQ) meloxicam SR

(4 μg/g), and local SQ lidocaine (3 μg/g). We then cut off the longer hair from the top of the animal's head and apply a depilation cream (Nair hair-remover lotion, Church & Dwight Inc.) around the planned incision site. We massage the depilator cream into the hair and wash it off together with the detached hair using alcohol after 30 s. We then clean and sterilize the skin by repeating a two-stage scrub with betadine and 70% ethanol 3 times. After cleaning and sanitizing the skin, we move the animal to the nearby surgical sterile site without interruption to the animal's plane of anesthesia. We then stabilize the animal's head using earbars. We use a 10 mm opening in the implant to pressure-mark the edges of the intended cut in the skin. We cut a circular piece of skin using scissors by following the previously marked trace. We then remove all the connective tissue remaining on the skull and cut the muscle pockets on both lateral sides of the skull. This step is most prone to result in multiple muscle bleeders, especially during the early stages of learning this procedure. During this step, and throughout the rest of the surgery, we use surgical absorbent gelfoam (Surgifoam 1972, Ferrosan Medical Devices) to control and stop any bleeders. At the surgery's start, we soften the gelfoam with just enough saline to avoid it becoming oversaturated. Throughout the entire surgery, we use only the gelfoam softened by saline. Next, using the surgical blade, we make densely distributed surface scrapes in the skull at the top and on the sides of the muscle pockets, and then etch the same skull surfaces using the dentin activator (Universal Dentin Activator Liquid S393, C&B-Metabond®, Parkell) for 10 s followed by a wash off with saline. Scraping and etching are important steps to ensure reliable long-term bonding of the dental cement to the skull and attachment of the implant. We then mark the bregma and the location of somatosensory cortex's hind-limb area (S1HL, AP = 0.5 mm and ML = 1.5 mm) relative to bregma. Using a 3 mm disposable biopsy punch (ear punch, 19D23, INTEGRA Inc.), we gently scrape the surface of the skull to mark out a 3 mm ring for drilling a craniotomy centered on S1HL. We use a Neoburr drill bit (FG ¼, Microcopy) for the initial drilling of the skull through 50% to 75% of the skull's thickness. We drill through the rest of the skull in gradual pecking motion using a beveled cylinder drill bit (1812.8F, Microcopy). After completing every full drilling circle, we apply saline to prevent overheating and flush away the bone chips. Once the craniotomy piece of the skull starts moving with brain pulsations, we remove this bone piece using forceps. We then clean the exposed brain from any blood, CSF, and bone chips using a piece of gelfoam. From this point in the surgery, we always make sure the brain never dries out and is moist with saline. We maintain adequate moisture by regularly pouring saline over the craniotomy and keeping the craniotomy covered with gelfoam for longer periods of time. We then take a sterile insulin syringe (1144303, 0.5 mL 28 G, BD Insulin Syringe, Belton, Dickinson and Co.) and bend the tip of 31 G needle by gently tapping the needle against a flat hard surface. This modified syringe serves as a hook tool for dura removal. We use this syringe with the hook to make 2 to 3 cuts in the dura mater for the upcoming viral injections. We let the brain stabilize after the durotomies while preparing for the viral injections.

We pulled glass pipettes (5-000-1010, DRUMMOND WIRETROL, Drummond Scientific Co.) using a Model P-97 (Sutter Instrument Co.) micropipette puller. We cut the tips using Vannas scissors under the microscope to the tip diameter of 25 to 50 μm. We fill the pipette's back with mineral oil (O121-1, 148223, Fisher Chemical Inc.) and its front with the virus, using the injector (53311, Quintessential Stereotaxic Injector, Stoelting Co.). We injected Cacna1h$^{Chr2EYFP+/-}$ animals with 500 to 750 nL of AAV2/9-CaMKIIa-GCaMP6f-P2A-nls-dTomato (Canadian Neurophotonics Platform Viral Vector Core Facility, RRID:SCR_016477) to the depths of 150 to 250 μm. We injected Trpv1$^{Chr2EYFP+/-}$ animals to the depths of 150 to 250 μm with 500 to 1500 nL of cocktail mixtures of AAV2/9-CaMKIIa-GCaMP6f-P2A-nls-dTomato and AAV2/9-syn.NES.jRGECO1a.WPRE.SV40 (Addgene, catalog No. 100854-AAV9) with GCaMP:jRGeCO proportion of 1:1. The same procedure was followed for BL experiment in wild type mice reported in Fig. 12(c) by replacing GCaMP-encoding AAV with AAV2/9-hSyn-C1-mNG-CaBLAM(APD3A6-ISN) (provided by Hochgeschwender lab at Central Michigan University) (Fig. 4). We mixed two AAVs and the green food dye (Fast Green FCF Solution, 26053-02, Electronic Microscopy Sciences Inc.) by releasing and withdrawing the mixture 2 to 3 times with a micropipette. We add green food dye to aid visualization of the flow of AAV during the injection. We insert the pipette into the brain using a stereotactic manual micromanipulator. We wait for 3 min after inserting the pipette to the targeted depth to allow

tissue to stabilize and we inject the AAV at the rate of 60 nL/ min. Following the injection, we wait for 5 min to allow the tissue to stabilize before withdrawing the pipette.

Once all 2 to 3 injections are completed, we cover the brain with the glass window. We make our glass windows by gluing together 3 mm (CS-3R, 64-0720, Warner Instruments Inc.) and 5 mm (CS-5R, 64-0700, Warner Instruments Inc.) circular coverslips using the optical adhesive (Optical adhesive 71, Norland Products Inc.). The 3 mm coverslip fits relatively snugly into the craniotomy, forming a tight seal against the drilled skull. This is important to minimize any risk of bone bleeders during the healing and to delay the overgrowth of craniotomy with dura and bone. We press the glass window into the brain using a basic custom pressure applicator with a diameter of 2 mm mounted on a stereotactic manipulator. Once the glass window is tightly pressed into craniotomy, we secure the window in place by applying a three-component dental cement (C&B-Metabond®, Parkell) around the circumference of the window. Before applying the dental cement to the skull, we add a black paint to the three-component dental cement mixture to reduce autofluorescence of the dental cement. Once we apply the dental cement around the circumference and the dental cement begins to harden, we withdraw the pressure applicator and start applying the dental cement throughout the rest of the skull. We also fill up with dental cement the muscle pockets that we make at the beginning of the surgery. Next, we cover the bottom of the implant with uncured dental cement mixture and place the implant on the skull centered over the cranial window. We then apply the dental cement mixture from all four sides of the implant to increase the security of its attachment to the skull. We also pour some dental cement mixture through the four holes atop of the implant that are used for attaching the screws during the spinal cord surgery below. Finally, we apply tissue adhesive (Gluture, Zoetis Inc.) throughout the perimeter of the dental cement to double secure the attachment of the dental cement mixture to the skull and the skin.

2.3.2 *Surgeries for spinal cord AAV injections and window implantation*

We perform spinal cord AAV injections and window implantations as part of a single surgical procedure. In our hands, the full procedure on average required 3 to 5 h plus 1 to 2 h of preparation time depending on the specific parameters of the AAV injections and specifics of any given animal. This procedure was developed by the right-handed surgeon and might require small modifications to achieve the optimal timing for the left-handed surgeons.

All surgeries follow the aseptic techniques. We anesthetize the animal using 1.5% to 2% isoflurane delivered in 100% USP-grade oxygen and exhausts collected using vacuum. We maintain the animal's body temperature stable throughout the surgery using a heating blanket and protect the animal's eyes using sterile ocular ointment. We prepare the animal in a nonsterile area before moving it to the sterile stereotactic frame. For the chronic spinal cord surgeries, we use the same stereotactic setup and injection tools as for the brain surgery, except we add a stack of breadboards (Thorlabs Inc.) with XYZ manipulators (60 mm × 60 mm footprint available from Amazon) needed for spinal cord manipulation. The spinal cord clamp holder posts used for all our surgeries were 220 mm in length. The original design by Farrar et al. included the spinal cord clamp holder posts 50 mm in length. We significantly increased the length of the implant holder posts to accommodate the dimensions of our stereotactic frame used for brain surgeries (Kopf Inc.). There were no particular benefits for using longer clamp holder posts. However, in our hands, the use of XYZ manipulators rather than hand-manipulation like in Ref. 10 yielded finer control over the implant position and simplified the transfer of knowledge between the students by simplifying this complex procedure.

After moving the animal from the induction chamber to the prepping station, we inject the animal with IP dexamethasone (0.2 μg/g), SQ buprenorphine SR (0.75 μg/g), SQ glycopyrrolate (0.5 μg/g), and local SQ lidocaine (3 μg/g). We then generously shave the animal's back using an electrical buzzer and apply a depilation cream (Nair hair-remover lotion, Church & Dwight Inc.) around the intended incision site. To determine the depilation area, locate the apex of the vertebral column's curvature and the last rib's position. The apex of the vertebral column curvature corresponds to the Th13 vertebrum.[60] Using a cotton swab, we thoroughly massage the depilator cream into the animal's back to cover all hair. After 30 to 60 s, we remove the loosened hair with a razor blade. Using alcohol pads, we meticulously remove any residual depilator cream

and detached hair. Using a two-stage scrub of betadine followed by 70% ethanol, we clean and sterilize the exposed skin, repeating this process 3 times. After this, we move the animal to the surgical stereotax for the sterile parts of the procedure.

To ensure the spinal cord clamps on the custom holders can reach the spinal cord's XYZ position, we align the animal's back with the XYZ manipulators. We then prepare the surgical gelfoam by soaking it in sterile saline. Next, we identify the skin incision site by palpating the ribs near the vertebral curvature's apex. Palpation typically involves sweeping the back with the fingers and holding them around the suspected last rib to detect its movement during breathing. The last rib emanates from the rostral end of the Th13 vertebrum.[60] For the imaging of the spinal cord at the vertebral level L1, we usually aim to have the skin incision that starts about 1 to 3 mm rostrally relative to the entry point of the last rib, covers the width of the implant (10 mm), and extends 1 to 3 mm caudally (i.e., 12 to 16 mm total). As was described in Ref. 10, it is possible to obtain a good quality spinal cord window even with a significantly larger skin incision. However, it is important to minimize any tissue damage and trying to tailor the incision size toward the implant's size does not have a significant impact on the duration or complexity of the surgery. For the imaging of the spinal cord segments under the L2 vertebrum, the skin incision should be moved caudally by 2.5 to 3.0 mm. After making the skin incision, we palpate the last rib again with forceps (Fine Instruments Inc.) to precisely locate Th13's rostral end. Once we locate the root of the last rib, we incise the soft tissue overlying the vertebra. The length of the cut is equivalent to the width of the implant. We begin by making a straight cut on the right side as close to the midline as possible while not cutting through the spinous processes. We turn the surgical blade more than 70 deg to align it nearly horizontally. Then we cut laterally toward the right to remove the overlying soft tissue. After reaching the transverse processes, we reorient the blade vertically and dissect away the tissue off the vertebral bodies not deeper than the thickness of the spinal cord bars (1.5 mm) to offer enough space for fitting the spinal cord bars under the spinal cord processes flush against the vertebral body. Similar to Farrar et al., the implant bars merge together three vertebrae. Hence, we clean up the lateral surfaces of three vertebral bodies, as well as cut off the tendons attached to all three vertebral bodies to minimize the motion during post-surgical imaging. After cleaning the lateral sides of vertebral bodies, we clamp the vertebral column from both sides with the spinal cord bars. We align the center of the bars with the approximate center of planned laminectomy over the middle vertebrum. We apply a generous amount of pressure to keep the spinal cord in place during the surgery and to promote strong chronic attachment via pressure after the surgery. Next, we partially trim away the spinous and transverse processes to maximize the flatness of the implant chamber against the vertebral bodies. The processes are not removed entirely, rather they are flattened by cutting away the superficial parts of the processes while keeping as big parts of the processes as possible to minimize tissue damage and promote strong attachment of the spinal cord bars. In our practice, it is best to cut the processes as early as possible because this step is prone to bone bleeding if done improperly and by cutting the processes early, the tissue has a longer time for coagulation before further cuts must be made. Next, we clean up the intervertebral spaces from all the connective tissue to have a clear tactile and visual feedback on the extents of the middle vertebrum. Once we know the extents of the vertebrum, we perform a laminectomy using a drill actuated via compressed nitrogen (both diamond burr and ball drill work well for this step). We sequentially drill longitudinally as far laterally as possible first on one side, then on the other and repeat switching sides after every pass, removing thin layers of bone on every pass until the bone becomes thin enough to be pulled up without having to apply a significant amount of force. Between every pass of the drill we apply the sterile saline to protect the spinal cord from drying.

After the laminectomy, we perform the viral injections following the same steps as for the brain injections. The main difference between the brain and spinal cord viral injections in our experience is that the spinal cord meninges are much harder to pierce through compared to the brain meninges. Hence, we performed durotomies for every spinal cord injection. The examples of pinching responses in Fig. 8 involved injections of an AAV2/9-CaMKIIa-GCaMP6f-P2A-nls-dTomato (Canadian Neurophotonics Platform Viral Vector Core Facility, RRID:SCR_016477) virus at 60 nL/ min. We administered the AAV via two injections on the right side of the spinal cord at 150 and 250 μm depths and one injection on the left side at 200 μm.

2.3.3 *Multiorgan surgeries as a single or two separate procedures*

When performing two independent surgeries within the same animal, each procedure is performed exactly as outlined above. The main important factor to consider is that the animal requires at least 3 days to recover after a brain or spinal cord surgery. We performed the second surgery 7 days after the first surgery out of an abundance of caution. Further, we typically performed brain surgery first followed by the spinal cord surgery. This choice was based on our experience with maintaining the good quality and responsiveness of surgerized neocortex across months without significant challenges with good consistency between the animals. Hence, the risk of the cranial window to decrease in quality while waiting for the spinal cord window (e.g., waiting for healing or viral expression) is lower than the risk or the amount of unavoidable quality change for the spinal cord window.

In the case of both brain and spinal cord surgeries performed as part of a single procedure, we follow the same surgical steps as outlined above except in all surgical cases the animals did not receive any viral injections in either of the sites. This was due to the significant surgical duration and the impact on the animal's health when trying to incorporate AAV injections into the surgery. The duration of a combined surgery in our implementation is at least 6 h. We typically would start with a spinal cord implant first and then would proceed with the brain implant. This choice is based on the fact that the spinal cord surgery is more prone to failure and if the spinal cord surgery is done following the brain surgery, the resources invested into brain surgery would be wasted.

As part of the development of surgical methodology, it was important to ensure that the surgical developments presented in this report are transferable to other scientists. The transferability of principles described here was validated by training a medical student on brain–spine surgeries. The transfer of knowledge could be efficiently performed following the knowledge and materials developed throughout this work and trained student was able to successfully perform the surgery toward collecting the data presented in Fig. 9(a).

2.4 Fluorescence Imaging

2.4.1 *One-photon imaging using electron multiplying gain CCD camera*

The results shown in Fig. 9(b) were imaged using an electron multiplying gain CCD (emCCD) camera (emCCD Ixon 888, Andor Inc. with LUCPLFLN20X 20× 0.45NA air objective). For imaging calcium using a green FL protein-based genetically encoded calcium indicator (GCaMP) and the blood vessels labeled with the fluorescein isothiocyanate (FITC) dextran [Figs. 9(b) and 10], the emCCD camera was equipped with GFP filter cube (DFM1 with GFP excitation and emission filters and dichroic, ThorLabs) and an excitation light-emitting diode (LED) (M470L3, ThorLabs Inc.).

2.4.2 *Two-photon imaging*

All the two-photon imaging was done using a custom microscope assembled by Bruker Inc. Vascular imaging data shown in Fig. 10 were collected using a 960 nm excitation laser wavelength with galvo scanning and 16× water immersion objective (0.80 W, DIC N2, Nikon LWD). Brain calcium imaging data shown in Fig. 9(c) were collected using a 980 nm excitation laser wavelength with galvo scanning and 10× objective (HC PL APO 0.40 NA, 506511, Leica Inc.).

2.4.3 *Imaging using miniscopes*

All the miniscope imaging was performed using UCLA miniscopes v4.0, v4.40, and v4.41. Miniscope v4.0 was generously provided by UCLA, v4.41 was purchased from OpenEphys, and v4.40 was purchased from OpenEphys. v4.40 miniscope from LabMaker offered the smallest amount of bleed-through excitation light noise and best imaging quality. Miniscopes v4.40 and v4.41 had the lens configuration 1 (combination of lenses 45-089, 45-089, and 45-691 from Edmund Optics with working distance 675 μm $\pm$ 250 μm and FOV of 1 mm $\times$ 1 mm) [250] and was used for brain and skin imaging. Miniscope v4.0 had the lens configuration 3 (combination of lenses 45-090, 45-090, and 45-691 from Edmund Optics with working distance

2010 μm $\pm$ 400 μm and FOV of 1.3 mm $\times$ 1.4 mm) and was used for spinal cord imaging. We tested the lens configurations 1 and 2 (working distance for configuration 2 is 975 μm $\pm$ 340 μm) for spinal cord imaging in multiple animals, but the working distance was too short for imaging using the window design and viral injection depth combinations used in this work. In 90% of the cases, all lens configurations allowed us to at least reliably image the cortical blood vessels.

For the imaging under anesthesia, the miniscope was attached to the implant chamber using 1 implant screw and for the awake imaging using two screws. We also imaged anesthetized animals implanted with the stainless-steel headposts and cranial windows not designed for the attachment of the miniscope. During these imaging sessions, the miniscope was mounted in a 3D-printed holder and positioned over the cortex using micromanipulators.

2.4.4 *Vascular imaging using dextrans*

Blood vessel imaging reported in Fig. 10 relied on labeling the blood vessels using injectable FL dextran dyes. Dextran was delivered into the animal's body via tail vein injection by hand using an insulin syringe (UltiCare U-100, #09335, ULTIMED Inc.). FITC green 10 kDa (D1821, ThermoFisher Scientific Inc.) dextran was delivered as a 30 μL of dextran solution mixed with 70 μL of sterile saline. Two-photon imaging setup used for vascular imaging in the spinal cord is summarized in Fig. 6(a).

2.4.5 *Behavior for fluorescence imaging experiments*

The awake imaging results reported in Fig. 9(c) required the animal to follow the seven-step behavior procedure summarized in Fig. 5. The steps were as follows.

(1) Handling

   (a) Handling helps to improve an animal's collaborativeness throughout the experiments. Given how sensitive the spinal cord preparations can be depending on the study and surgeon's technique, as well as the complexity of multisite surgical procedures, it can be beneficial to assess an animal's collaborativeness ahead of the first surgery. Animals that within 3 to 5 days do not become significantly better at collaborating with the researcher and do not increase in comfort of being handled, it can be beneficial for animal's health and the experiment to assign a given animal to the acute track or invest additional time to increase the chances for a given animal's successful participation.
   (b) Handling helps to maximize the animal's comfort with the experiment, minimize the risk of tissue damage, increase the experimental duration, and overall, improve the quality of data.
   (c) Increasing the animal's comfort with being handled by the researcher is especially critical for maintaining the longevity of the spinal cord implants. Even miniscope imaging requires restraining or anesthetizing the animal for 2 to 5 min to attach the miniscope. Hence, by the first time of needing to attach a miniscope, the animal needs to be comfortable with being held in place by the researcher.

(2) Surgery 1

   (a) This can be either a brain or spinal cord surgery.
   (b) This could also be a single brain–spine surgery. However, as part of this study, the animals following a single brain–spine surgery received stimulation only under anesthesia and were imaged awake only when looking at the changes in brain–spinal activity during the transition from anesthetized to awake state. Hence, single multisite surgery animals did not follow the behavior protocol for awake study.

(3) Handling and imaging

   (a) Between the surgeries, it is important to continue handling the animal to increase their comfort with the researcher despite the invasive procedures. A good assessment metric for determining the endpoint for handling can lie in achieving collaborative

behavior qualitatively comparable to the behavior after the initial handling prior to the first surgery.

(b) At this stage, it can be useful to image through the implanted window to verify the ability to see the target signal. However, if not sufficient time has passed since the first surgery (e.g., at least 2 weeks for the AAV2/9-CaMKIIa-GCaMP6f viral expression used in this study), the lack of signal or responsiveness to sensory stimuli might not be informative about the prognosis for the signal strength.

(4) Surgery 2

(a) This can be either a brain or spinal cord surgery.

(5) Habituation

(a) This step consists of three substeps.

(b) Habituation to the head restraint for 1 to 2 days, gradually increasing the duration between 5 to 10 min.

(c) During the next 1 to 2 days, add *ad libitum* sucrose (30%) and brain imaging to gently promote the animal's continuous acclimation to the parts of the experimental setup. As part of this step, continue increasing the duration of restraint toward 15 to 30 min. The microscope in this case contributes only the excitation light and it might be beneficial to avoid attempting to image during the habituation to avoid photobleaching. However, we find it useful to start imaging the brain at this earlier stage because the cost of imaging is low (data storage and experimental time), but the efforts to image at this stage help to learn the particular brain landmarks and probe the responsiveness of different areas.

(d) Add hindpaw restraint and optomechanical stimulation as the final parts of the experiment. Continue increasing the duration up to 60 min. Continue habituating until the animal develops comfort with the needed number of trials or the animal stops improving in its performance. The performance in this case is assessed by the amount of animal's motion and signs of not wanting to continue engaging with the experimental setup. For the purposes of sensory optogenetic and mechanical stimulation experiments (Fig. 9), the minimal number of trials was 60 (up to 12 min) to allow at least 30 trials of optical and 30 trials of mechanical stimulation.

(e) As part of this study, we strongly considered the idea of habituating the animals to head-restraint during between the first and second surgery. The benefit would be that the animal learns the behavior before any serious interventions and in theory it should be easier for the animal to learn the task after the first surgery than after both surgeries and relearn the task after the second surgery rather than learning it from zero after the second surgery. Albeit, this approach seems promising, it has not been tested as part of this study.

(6) Imaging

(a) Imaging involves the use of the same full behavior as the last habituation step. The only difference is the addition of the microscope to image either from both sites or continue image from a single site depending on the experimental goals.

(7) Acute experiment

(a) As the final step, the animals typically undergo the acute experiments relevent for studying the question of interest (e.g., in the case of studying nociceptive information processing, such experiments can involve capsaicin injections[12] followed by mechanical and optogenetic stimulation).

Ultimately, this procedure is animal-specific and all the durations provided in this procedure might have to be adjusted for a particular animal's phenotype. In addition, given the high value of double implant animals, in the rare cases of brain implant detachment during the habituation, it is possible to reattach the implant. However, it is important to start the surgery immediately to moisturize the brain as soon as possible. The quality of the craniotomy will inevitably

decrease in the case of reimplants, hence it is justified to perform this step only in the cases of animals showing exceptionally strong responses. We have not tested spinal cord reimplantation because of the lack of cases of implant detachment. However, given the propensity of the spinal cord toward bleeding and the involvement of silicone elastomer when creating a spinal cord window, the impact of spinal cord reimplantation can be predicted to be inevitably significantly more severe than in the case of brain and will likely be associated with the spinal cord injury.

Animals that were not involved in any awake behavior as part of this study (e.g., the animals participating in the spinal cord endogenous light sensitivity study) did not undergo handling, habituation, and awake imaging.

2.5 Bioluminescence Imaging

2.5.1 *Bioluminescence imaging under anesthesia*

BL imaging under anesthesia was performed using topical administration of luciferin (water-soluble h-Coelenterazine, #3011, NanoLight Technologies) atop of exposed cortex. Cortex was exposed by removing a chronic glass window implant immediately before imaging [Fig. 4(a)]. Wild type animals imaged under anesthesia received either the injection of pAAV-hSyn-Kozak-NCS2 [Fig. 12(a)] or AAV2/9-hSyn-C1-mNG-CaBLAM(APD3A6) [Fig. 12(b)]. When imaging CaBLAM(APD3A6) using BLmini v2.0 [Fig. 12(b)], the animal was receiving mechanical stimuli of vibrissa.

2.5.2 *Bioluminescence imaging in awake behaving animals*

BL imaging in awake behaving animals was performed following a systemic administration of luciferin (fluorofurimazine, N410A, Promega Corporation) via intraperetoneal (IP) injection [Fig. 4(b)]. Wild type animals in this experimental group received injections of 1:1 mixture of

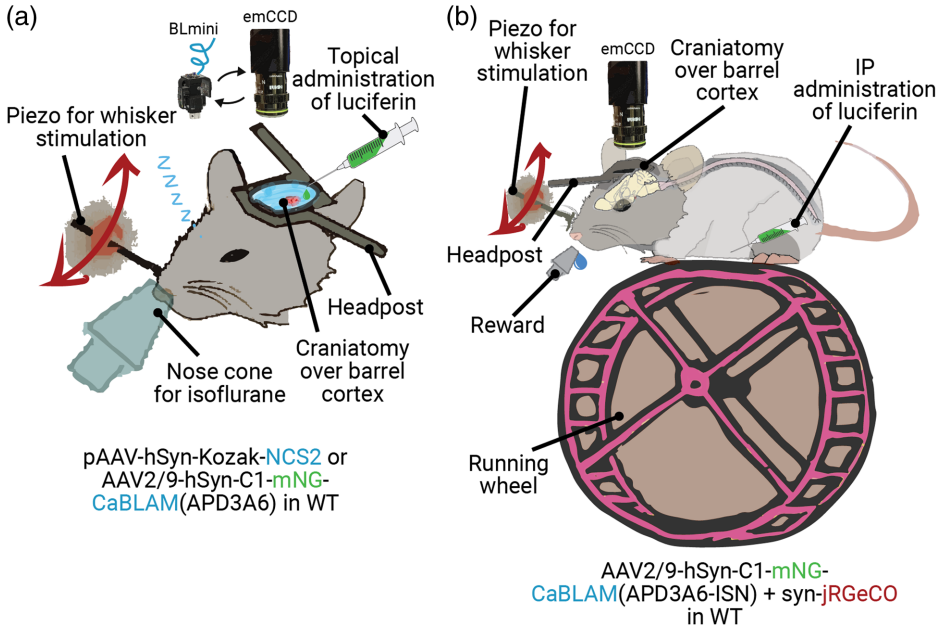

Fig. 4 BL imaging was conducted in anesthetized animals with direct cortical luciferin application and in awake behaving animals with systemic injection. (a) We performed acute BL imaging under isoflurane anesthesia with direct cortical administration of luciferin (coelenterazine). The same preparation was used for imaging either using an emCCD camera or the BLmini. During the experiments testing novel BL calcium indicators [e.g., CaBLAM (APD3A6)], we stimulated vibrissae using a piezoelectric element. (b) For awake BL and FL (e.g., jRGeCO) imaging, we administered luciferin intraperitonially (IP) before headpost-restraining the animal on a running wheel. We imaged BL and FL through the same cranial window sequentially to compare relative activation profiles.

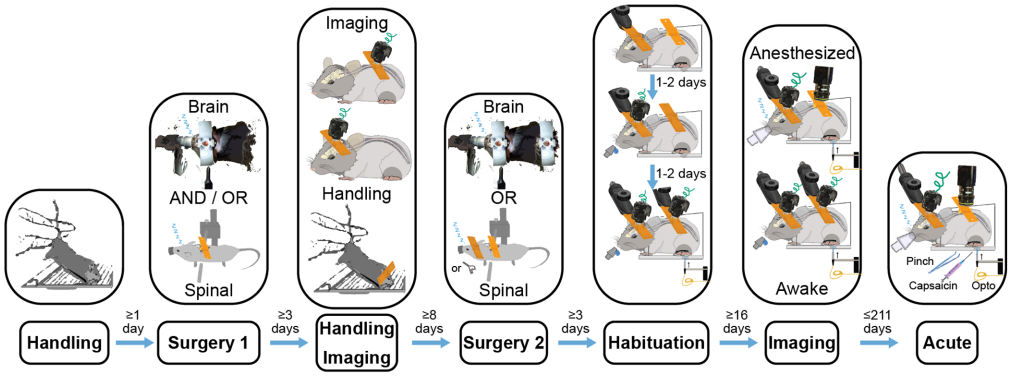

Fig. 5 Timing of steps that enable awake simultaneous brain–spinal cord imaging awake imaging simultaneously in the brain and spinal cord to study sensory information processing requires careful design of a multistep animal training protocol to maximize animal comfort and data quality.

AAV2/9-hSyn-C1-mNG-CaBLAM and AAV2/9-syn.NES.jRGECO1a.WPRE.SV40 (Addgene, catalog No. 100854-AAV9) into SI Vibrissal Barrel Neocortex. IP injections were performed at a procedure station away from the imaging setup. After the IP injection, animal was head-restrained on a running wheel with unlimited supply of sucrose solution. Imaging was initiated within five minutes following the IP injection.

Following the identification of the fluorescence expression area, either jRGeCO or CaBLAM(APD3A6-ISN) was imaged sequentially while applying stimulation of vibrissa. Imaging of jRGeCO was performed using tdTomato filter cube and no filters were used for imaging CaBLAM(APD3A6-ISN). For these experiments, the emCCD camera (emCCD Ixon 888, Andor Inc.) was equipped with a 5x air objective (378-802-6, Edmund Optics Inc.).

2.6 Stimulation

2.6.1 *Pinching*

Pinching responses were evoked by gently squeezing the hindpaw with the hand-held forceps. The effort was made to apply the pressure consistently at the same location. However, the amount of pressure exerted by every pinch varied pinch-to-pinch because of natural variability present when manually delivering somatosensory stimulation.

2.6.2 *Optogenetic and mechanical stimulation of the hindpaw*

All plantar hindpaw optogenetic stimulation experiments were performed using 470 nm LED (M470F3, ThorLabs Inc.) controlled using an LED driver (LEDD1B, ThorLabs Inc.). Light was delivered to the plantar hindpaw using an optical fiber. The stimulated hindpaw was covered with the black aluminum foil to minimize light propagation beyond the stimulation target. The cannula of the optical fiber was glued using epoxy to the piezoelectric plate bender (CMBP09, Noliac Inc.) to allow interleaved mechanical and optical stimulation trials. The mechanical stimulation was done by poking the animal's plantar hindpaw with the optical fiber's cannula by actuating the piezoelectric plate bender via an amplifier. An example of the stimulation waveform parameters is shown in Fig. 6(b).

Imaging and optomechanical stimulation were controlled and synchronized using either an OpenEphys or National Instruments (NI BNC-2110, NI PCI-6713, and USB-6008 for emCCD and BNC-2110 with PCIe-6353) data acquisition boards operated via MATLAB R2015b and OpenEphys software v0.5.5.3.

2.6.3 *Optical stimulation of the spinal cord*

The optogenetic stimulation of the spinal cord was performed by directly aiming an optical fiber at the spinal cord implant [Fig. 6(a)]. The important aspect of spinal cord optical stimulation was the use of flyback to reduce the artifacts during two-photon imaging. Even though the imaging

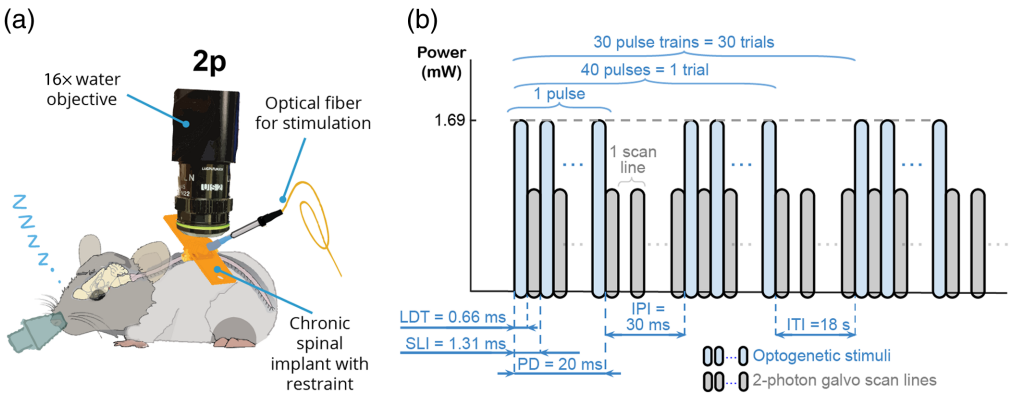

Fig. 6 Spinal cord photomodulation approach integrated with two-photon imaging. (a) We performed optical stimulation in the spinal cord under isoflurane anesthesia through a chronically implanted spinal cord window using an optical fiber positioned adjacent to the imaging objective. (b) We imaged spinal cord vascular responses using two-photon galvo–galvo scan mode. The use of two-photon galvo–galvo allowed us to minimize the optical stimulation artifacts by flashing the stimulation LED only during the scanner flyback between the scan lines; see Ref. 61 for further details. LDT, line dwell time; SLI, scan line interval; PD, pulse duration; IPI, interpulse interval; and ITI, intertrial interval.

approach used for collecting the data reported in Fig. 10 relied on GFP filters that should block 470 nm light used for stimulating the spinal cord, the imperfect stopband of the filters and high sensitivity of two-photon photomultiplier tubes (PMTs) results in artifacts when trying to apply optical stimulation during two-photon imaging. Flyback stimulation approach relies on the fact that galvo scanning requires pausing the imaging during the data collection with PMTs to mechanically reposition the scanner between the scan lines. The transition time between the scan lines is defined as the line period and the stimulation is applied only during this transition to effectively reduce the signal contamination with the photons reflected back into the objective from the stimulation beam (Fig. 6).

2.7 Image Analysis

All microscopy images have been processed using either ImageJ (Fiji, v1.53f51) or MATLAB R2021a (MathWorks Inc.). For all the multitrial analyses (e.g., Figs. 9, 10, and 12), the data as plotted as a percentage change of baseline (i.e., $dF/F\%$ change) activity during 1 s interval preceding the stimulus:

$$dF/F = \frac{\text{signal} - \text{baseline}}{\text{baseline}} \times 100\%, \tag{1}$$

where signal is data recorded during stimulation and baseline is data recorded during the time interval preceding stimulation.

In the case of individual pinch response data in Fig. 8, the baseline activity for each neuron was defined as the full experiment-averaged activity within the area surrounding each neuron.

2.8 Statistical Analysis

The analysis of animal weights reported in Fig. 7 relied on multiple comparisons using the Bonferroni method. The significance threshold was set to $p\,\text{value} < 0.05/300 = 0.00017$. The statistical analysis was performed using MATLAB R2021a (MathWorks Inc.).

3 Results

Here we aimed to compare multiple implant designs and surgical preparations to drive calcium flux and thus indicator fluorescence (e.g., mechanical touch, pinching, peripheral optogenetic stimulation, and local optical stimulation), as well as multiple imaging preparations (anesthetized and awake, wearable one-photon, benchtop 1 and two-photon imaging, sequential and simultaneous multiorgan imaging).

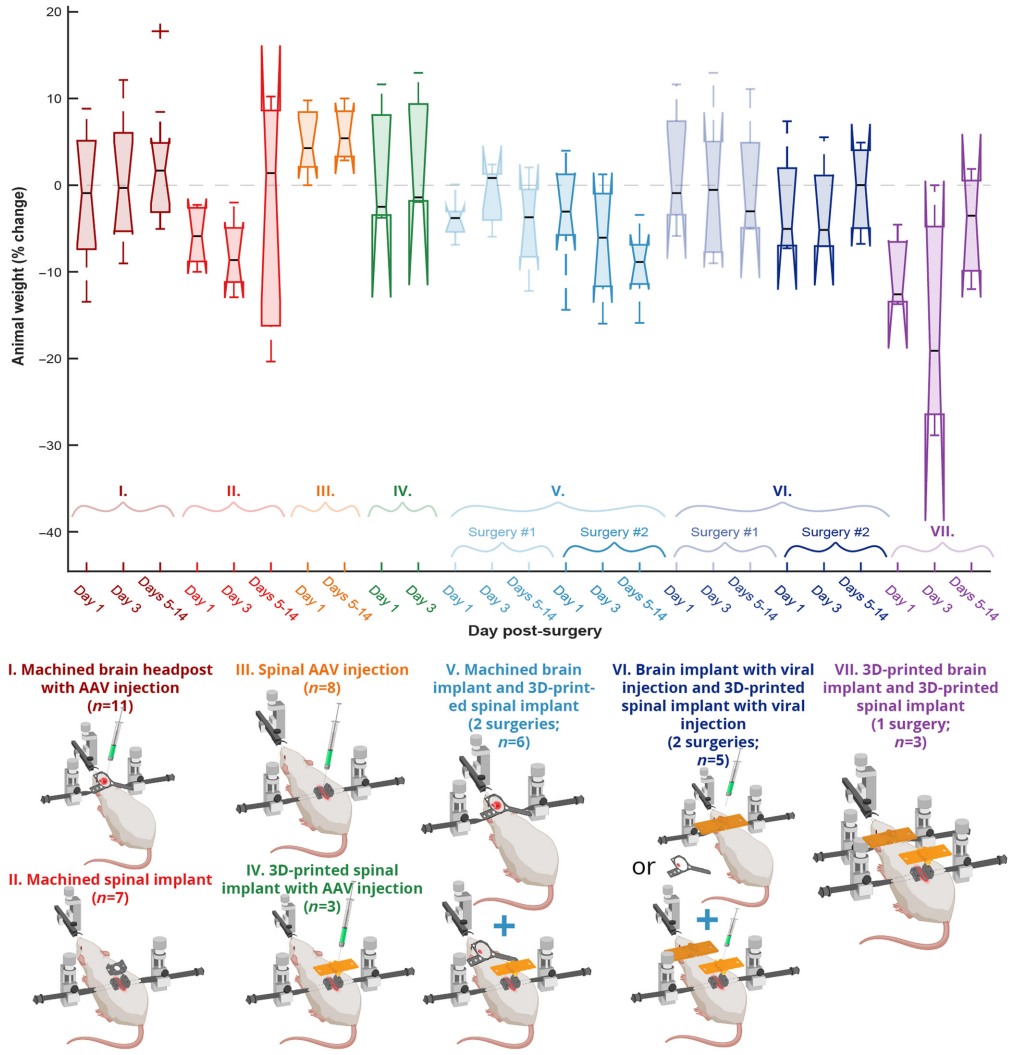

Fig. 7 Tolerance of the multiple implant variants tested. In all implantation approaches, animals appeared healthy upon observation, maintaining presurgical body weight or recovering within ~1 to 2 weeks. This figure was created partially with BioRender, Ref. 74.

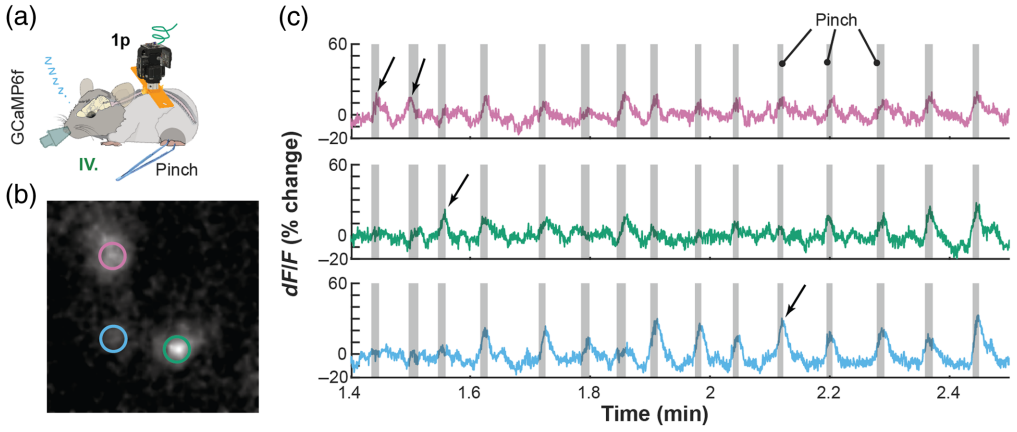

Fig. 8 UPRIM spinal cord implants are viable for single cell GCaMP imaging. (a) Individual cell GCaMP6f calcium responses to hind paw pinch were imaged under anesthesia in an animal implanted with spinal cord UPRIM via surgical procedure IV and using Miniscope v4. Calcium indicator was expressed via AAV2/9-CaMKIIa-GCaMP6f-P2A-nls-dTomato. (b) A pinch response map as the average of multiple trials, showing activation in multiple distinct neurons (pink, green, and blue circles). (c) Time series show changes in signal for each color-matched cell. Gray shadings highlight the pinching time intervals, arrows emphasize responses that differed between three cells.

3.1 Animals Tolerate the UPRIM 3D-Printed Implants in Several Configurations

Our exhaustive testing of various implant designs and surgical approaches revealed no discernible adverse effects on the health of the animals, based on qualitative observations of postsurgical markers and behavior, and quantitative tracking of animal weight. The implants and surgical combinations tested during this work included seven different preparations across 41 mice, summarized in Fig. 7. Our analysis identified no significant differences in weight trajectories between any of the compared groups when using a significant level adjusted for multiple comparisons (Multiple one-way ANOVAs, Bonferroni corrected, 300 surgical preparation pairs, $p > 0.05$). The surgical preparation groups were as follows:

(1) implantation of a machined brain headpost with cortical viral injections;
(2) implantation of machined spinal cord implant (design described in Ref. 10);
(3) spinal cord viral injection without implants;
(4) spinal cord 3D-printed implant with viral injection;
(5) implantation of machined brain implant (surgery 1) followed by implantation of 3D-printed spinal cord implant (surgery 2);
(6) implantation of machined brain implant with viral injection (surgery 1) followed by implantation of 3D-printed spinal cord implant with viral injection (surgery 2);
(7) implantation of brain implant and 3D-printed spinal cord implant in a single surgery.

3.2 UPRIM Spinal Cord Implants Are Viable for Single-Cell Imaging and Have Practical Advantages

Single-site imaging of spinal cord activity dynamics has proven challenging for several reasons: (i) high mobility of the spinal cord requires sophisticated motion correction algorithms and more complex surgical implant attachment designs; (ii) imaging depth is shallower than in the brain due to photon scattering by spinal myelination (Fig. 2); (iii) surgical procedures are more complex and hence require more training than brain procedures; (iv) the spinal cord has a smaller tool builder community than the brain, and advancements happen at slower pace; (v) in general, the longevity of spinal cord window implants is lower than for the brain; and (vi) the highly mobile structure of the spinal cord makes it challenging to design implants capable of withstanding traditional restraint paradigms used for brain imaging, limiting the complexity and number of experimental trials that can be performed under awake spinal restraint.[62]

Several crucial breakthroughs in overcoming these challenges have been led by Schaffer et al.[10,63,64] Their spinal chamber implant design and procedure revolutionized the field by allowing chronic two-photon imaging of the blood flow in spinal stroke[63] and changes of axonal morphology following spinal cord injury.[10] Building on this success, they have now also demonstrated the feasibility of imaging ventral spinal cord using three-photon microscopy.[64] Their work laid the foundations for several recent studies building on this original design that have in turn made important, unique contributions.[8,62,64]

Although recent progress has been substantial, prior spinal implant designs have limitations we sought to mitigate in our work. First, we found the process of restraining an awake animal using custom-fabricated fine screw-based holders time consuming and stressful for the animal when compared to the streamlined restraint process using our standard headpost implants. Second, we experienced significant variability in the quality of spinal window preparation, in part due to the need for a large amount of elastomer between the window and implant chamber.[10] Third, we wanted to image spinal cord in awake, freely moving animals. However, the only study that has succeeded at imaging spinal cord in awake animals as we were initiating this work was done by Nimmerjahn et al.,[8] and the path to adaptation to our experimental goals was unclear. Fourth, the original design reported by Schaffer et al. relied on potentially expensive machining and required significant time to machine in a professional workshop due to its fine dimensions and high hardness of the stainless steel required (316). We addressed these four constraints by the following means. First, to streamline the restraint, we adopted "restraint wings" from our headpost implant design that allow us to employ the same basic off-the-shelf clamps used for headpost restraint, and hence makes these methods easy to be adopted by any brain-focused labs. Second, to increase window longevity, we brought the glass window closer to the surface of the cord, as in our brain windows, avoiding the air gap along the midline and reducing

the amount of elastomer needed. Third, to facilitate spinal cord imaging in unconstrained animals and promote broader adoption, we added a screw holder collar for the widely adopted open-source UCLA Miniscope V4. Fourth, to decrease experimental costs and streamline our ability to iterate implant designs, we used 3D-printing, manual processing (gluing, sanding, drilling, and tapping by hand tools) and off-the-shelf components. Because we adopted many features for UPRIM from brain headpost design, the final design version presented here naturally is suitable for brain imaging as well. Importantly, this consistency across organs allows to use the same miniscope interchangeably for brain and spinal cord imaging. Here we present proof-of-concept imaging of robust single-neuron and rapid activity-specific dynamics (Fig. 8). Figure 8 shows three neurons imaged under anesthesia using the UCLA miniscope v4 during hindpaw stimulation 37 days after implantation and AAV injection.

Our initial imaging success (and see further examples throughout) is paired with a variety of other pragmatic benefits of UPRIM as a spinal implant system. First, as shown in Fig. 7, these implants are well-tolerated, even when multiple windows are in place. We observed no specific impact on body weight. Second, as described throughout, the UPRIM system is lightweight, at only 1.64 g compared to 1.96 g for the stainless still machined implant reported by Schaffer et al. (this weight includes the chamber, glass window, screws, and spinal bars). In the case of brain imaging, UPRIM weighs only 1.45 g, whereas commonly employed machined versions weigh 2.39 g (including restraint chamber and glass window). Altogether, a pair of UPRIM multiorgan implants would weigh 3.09 versus 4.35 g for machined implants, a 29% reduction. This UPRIM value includes the additional features necessary for miniscope attachment, which if added to the machined implants would increase their weight differential. Third, the UPRIM fabrication process is easier than custom machining, and because it does not require a professional machinist it is also cheaper.

3.3 Imaging Calcium Activity in the Brain and Spinal Cord with UPRIM

Single brain–spinal cord surgery allows chronic imaging of transgenic GCaMP6f responses for up to 15 days postsurgery [Fig. 9(a)]. Dynamic one-photon calcium responses of transgenically labeled somatostatin (SOM) interneurons were reliably localized to the side of stimulation for up to 154 days after the surgery. We also conducted sequential imaging from brain and spinal cord UPRIM under anesthesia [Fig. 9(b)] and simultaneously in awake animals (data not shown). In the example shown in Fig. 9(b), imaging of nociceptive responses following optogenetic stimulation in $Trpv1^{Chr2EYFP+/-}$ mice was first performed in the brain 24 days after surgical implantation with UPRIM. After 52 days, an additional UPRIM was implanted in the spinal cord, and the data shown acquired 76 days later. Plantar optical stimulation of the right hindpaw reliably evoked cortical responses to all stimuli except for the weakest stimulation (i.e., 0.28 mW). Ipsilateral plantar stimulation of the left hindpaw also evoked brain responses but of smaller (1% change versus 2.5% change for the strongest optical stimulus) and more sustained magnitude compared to the contralateral stimulation. In contrast, the spinal cord responded to mechanical plantar stimulation of the left hindpaw, with no detectable response to right hindpaw plantar stimulation.

3.4 Using UPRIM to Test Optical Activation of the Spinal Cord: Vasodilation of Spinal Vessels in response to Blue Light in Wild-Type Mice

Multiple studies have shown that blue light can, through an endogenous mechanism, drive dilation.[65,66] Using UPRIM, we tested that blue light (470 nm) induced vessel dilations in wild-type animals using two-photon imaging 24 days after spinal surgery (Fig. 10). We found reliable induction of vasodilation in several, but not all, vessels tested.

3.5 Bioluminescence Offers Benefits for Wearable Miniscopes: Smaller, Fewer Component, and Lower Power Consumption

Based on the advantages of BL imaging in general and several benefits to miniscope design conceptually possible, we developed a novel miniscope optimized for BL imaging, the "BLmini." Figure 11 summarizes characteristics of two generations of FL- and BL-targeted miniscopes. The signal strength comparison between FL v3.2 and BLmini v1.0 miniscopes was determined by measuring minimal detectable optical signal with two microscope configurations. The relative signal strength for FL v4 and BL v2.0 miniscopes was based on 5× increase in sensitivity

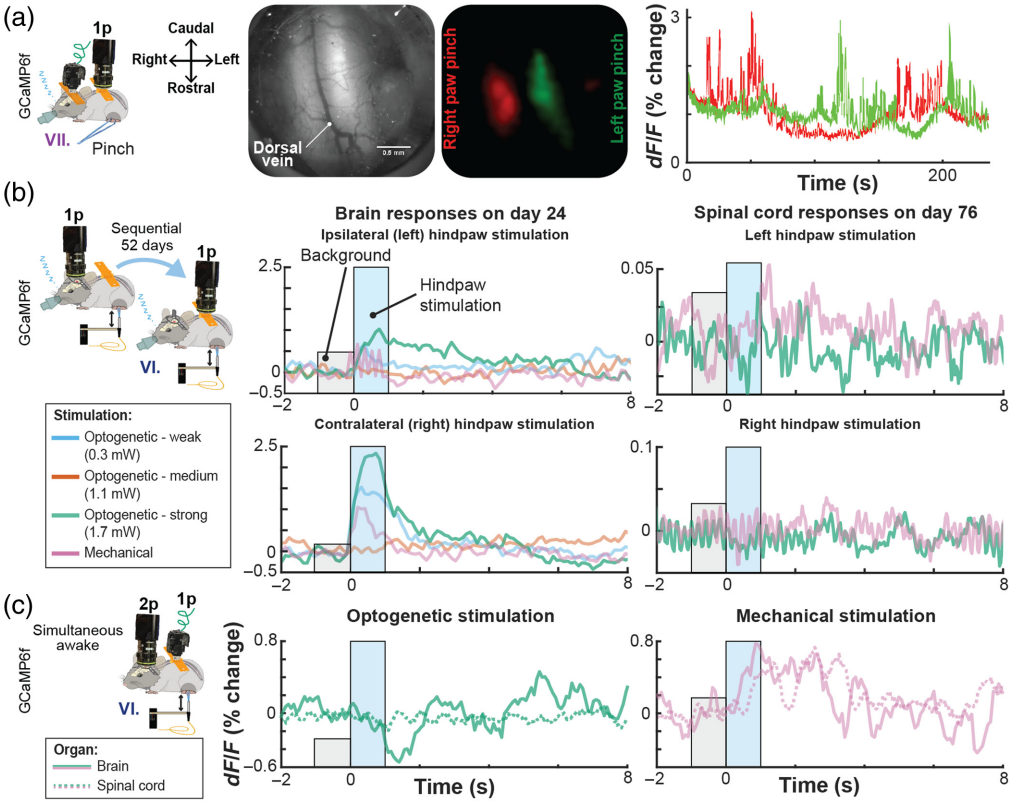

Fig. 9 Calcium activity in the brain and spinal cord in the same mouse using UPRIM. (a) Lateralized localization of responses to hindpaw pinch in the spinal cord using the UPRIM implant and 4× magnification benchtop imaging. The GCaMP6f indicator was expressed in Somatostatin-positive interneurons (SOM). Images in this panel from left to right show: the experimental setup with spinal cord reference axes for orientation, spinal cord brightfield image, GCaMP6f average response maps, and time courses showing the independence of relative light intensity signals for left (green) and right (red) cord regions. In this experiment, the mouse was implanted with a brain and spinal cord UPRIM (surgical procedure VII). (b) UPRIM calcium responses in cortex to optogenetic and mechanical stimulation 24 days after implantation, and in the same mouse (Trpv1$^{ChR2eYFP+/-}$) in the spinal cord 52 days after implanting and imaging brain UPRIM (surgical procedure VI). Both datasets were acquired under anesthesia. (c) UPRIM calcium responses imaged simultaneously in cortex and in the spinal cord in awake mouse (Cacna1h$^{ChR2eYFP+/-}$) following surgical procedure VI. In (b) and (c), animals were injected with a mixture of two nonflex AAVs to co-express GCaMP6f and jRGeCO both in the brain and spinal cord.

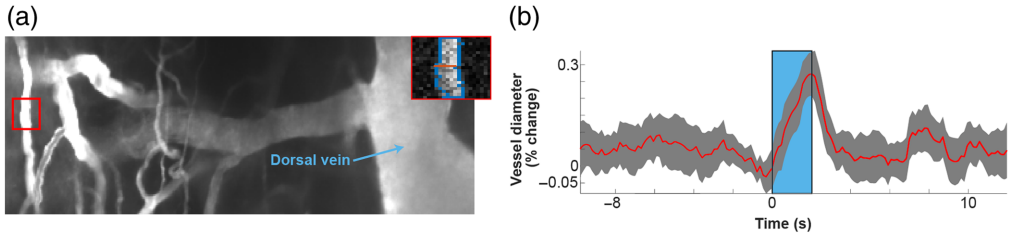

Fig. 10 Vascular dilations in the spinal cord in wild type mice driven by 2 s long trains of pulsed light. (a) Map of spinal cord vasculature obtained with two-photon imaging after intravenous 10 kD FITC-green dextran injection. Zoomed-in vessel inset in top right shows a single frame of a segmented vessel during stimulation. (b) Example of a responsive vessel segment.

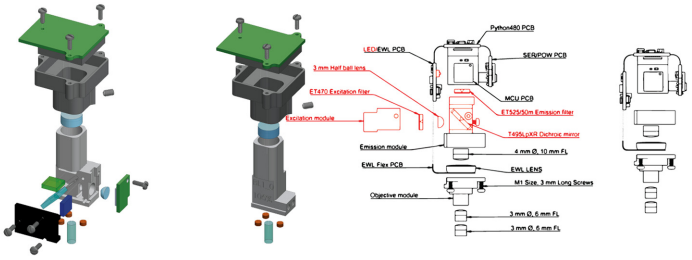

	UCLA miniscope v3.2	BLmini v1.0	UCLA miniscope v4	BLmini v2.0
Mass	3.2 g 6.7 g (wire-free)	2.5 g 5.7 g (wire-free)	2.6 g 5.8 g (wire-free)	~1.9 g 5.1 g (wire-free)
Number of components	22	12	22	15
Cost/scope	$1263 (1to4 scopes) $547 (≥20 scopes)	$526 (1to4 scopes) $443 (≥20 scopes)	$1190 (1to4 scopes) $890 (≥9 scopes)	$665
Signal strength	x @ 460nm y @ 530nm	~15x @ 460nm ~3y @ 530nm	~4.4x @ 460nm ~5y @ 530nm	~66x @ 460nm ~15y @ 530nm
Power consumption	1,100 mW (wired) 296 mW (wire-free)	957 mW (wired) 148 mW (wire-free)		
Sensitivity threshold	1.61 e/μm^2		0.96 e/μm^2	

Fig. 11 BL imaging requires fewer system components, decreasing miniscope complexity and weight conversion of UCLA miniscopes v3.2 or v4 from FL-centric to BL-centric design offers 22% to 27% reduction in mass, 32% to 45% reduction in the number of components and assembly labor, 19% to 58% reduction in cost/scope, 3 to 66 times higher sensitivity for optical signals that do not require filtering, 13% to 50% reduction in electrical power consumption. BLmini v2.0 compared to BLmini v1.0[59] offers up to 5 times greater signal sensitivity or 5 times shorter exposure time at 530 nm. This figure was modified with permission from Ref. 59.

of miniscope v4 compared to v3.2 shared with us by the miniscope developers. The power budget in Fig. 11 was estimated for a wire-free version of UCLA miniscope made public on 5/21/2019.

3.6 Using Miniscopes to Detect Bioluminescent Indicators

BLmini v1.0[59] and v2.0 were able to capture temporal dynamics of *in vivo* BL that tracked those observed using an electron-multiplying gain camera (emCCD Ixon 888, Andor Inc.) [Fig. 12(a)]. For comparison, we overlaid time courses acquired using the BLmini v1.0,[59] BLmini v2.0, and emCCD, each from a different experiment [Ref. 58; Fig. 12(a)]. The signal captured by the BLmini also tracked more subtle features of the known BL response. These properties include an early slowing in photon production during substrate injection, thought to be due to the inhibition of photon production by the breakdown products.

A difference between emCCD and miniscope signals is their baseline signal magnitude prior to the injection of h-CTZ. The CMOS sensor employed in the miniscope does not rely on any form of cooling and consequently suffers from significantly stronger thermoelectric background noise as well as anisotropic distribution of noise across the pixels. The most critical factor that helped us to mitigate these issues involved letting the miniscope to operate for 30 min (duration was determined empirically) before starting to image. This wait time does not reduce the noise; however, it offers a stable baseline for measurements.

Using the more sensitive BLmini v2.0, we were able to measure spatial maps of photons emitted by calcium-dependent BL indicator CaBLAM [Figs. 4(a) and 12(b)]. Further, BL indicators themselves are reaching the stage of development where we can image using emCCD camera sensory stimulation responses of comparable time course using BL and FL in the same preparation [Figs. 4(b), 12(c) and 12(d)].[55]

4 Discussion

The hardware and surgical advances we present here enabled observing "field" calcium and vascular dynamics in brain and spinal cord and from the same animal for up to 8 months (data

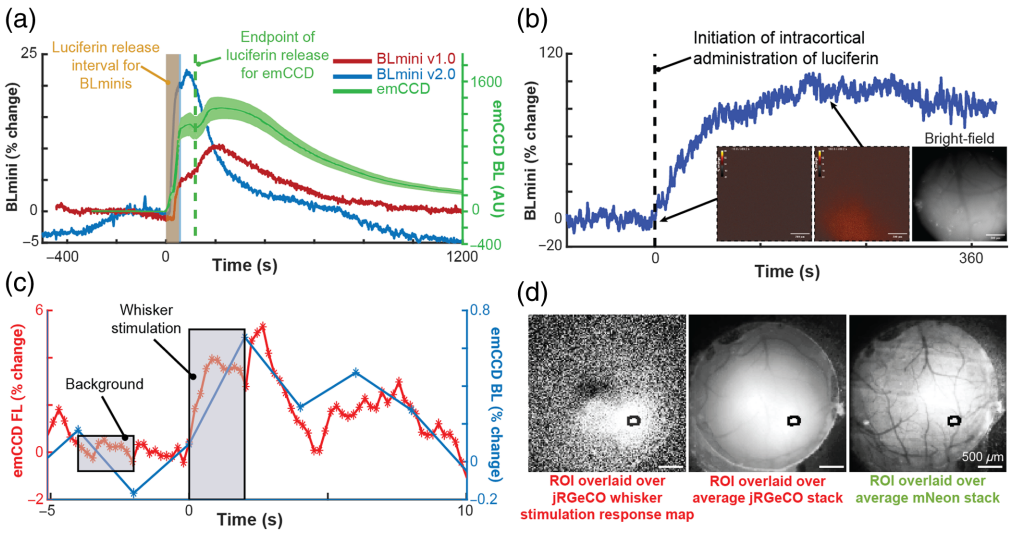

Fig. 12 Imaging BL and FL indicators using the BLmini and FL. (a) Time courses of BL photon production detected by an emCCD (ANDOR) and two generations of BLmini miniscopes in three different mice. Luciferin (CTZ) was directly applied to the cortical surface, previously transduced with either LMO3[58] (emCCD data) or NCS2[59] (BLmini data). (b) BLmini v2.0 allows detection of photon production by the calcium indicator CaBLAM (APD3A6) [Fig. 4(a)].[55] The insets from left to right: pre-hCTZ baseline signal, peak BL, post-BL bright-field image. (c) Time series for BL and FL calcium indicator output from a single imaging session, from CaBLAM (APD3A6-ISN) and jRGeCO (with full field excitation illumination) virally transduced in SI Vibrissal Barrel Neocortex (synapsin (Syn) promoter). In these data, vibrissal stimulation was applied during either BL (blue) or FL (red) imaging (25 trials in each condition) [Fig. 4(b)]. (d) The region-of-interest used to extract jRGeCO and CaBLAM (APD3A6-ISN) signals overlaid on the mean jRGeCO vibrissa response map (left), the mean red FL intensity map across all frames (center), and the mean green FL map, reflecting expression of mNeonGreen (mNG) in the CaBLAM (APD3A6-ISN) construct. Scale bars in all 3 images = 500 μm. This figure was modified with permission from Ref. 59.

not shown) after the first surgery. The novel design provides a well-tolerated, affordable, and common format for imaging the brain and spinal cord, in fixed and free-behaving mice. As such, this approach enables unique observations under conditions where each site is imaged individually but in the same mouse and on the same day, such as the time course of plastic changes in neural ensembles following a peripheral manipulation. The UPRIM strategy also enables unique correlational studies with simultaneous imaging across sites, for example, for determining the conjoint spinal cord and brain activity that may be key to nocifensive responses or detection of nociceptive stimuli.[67]

The main limiting factor for imaging individual cells across multiple sites was the longevity of the spinal cord window due to overgrowth. Our maximal duration for obtaining quality signals was 37 days after the spinal cord surgery. This finding aligns well with previous observations using stainless steel implants that resolved spinal cord axons for more than 35 days in only ~50% of implanted mice due to fibrosis.[10] Maintaining good surgical technique remains the best tool to increase the longevity of the spinal cord windows. In our experience, the key surgical priority is minimizing injury and bleeding. Other important factors leading to reduced insult to the spinal cord include: (i) sealing all bone edges throughout the laminectomy using tissue glue (e.g., VetBond); (ii) minimizing elastomer use (e.g., KwikSil; in the implant design we present here, this was achieved by positioning the glass window under the implant chamber, akin to traditional brain implant designs); (iii) increasing the pressure seal between the glass window and the spinal cord (akin to traditional brain implant designs); and (iv) using a pneumatic drill rather than a mechanical drill or scissors. Alternatively, reducing surgical invasiveness by imaging between the vertebrae prolongs the chronicity of spinal cord imaging for up to 167 days.[68] Also treating an implant with gradually releasing anti-inflammatory agents might increase the duration of single-cell resolved imaging by suppressing fibrosis.[62] In addition to surgical preparation, habituation of the animal remains an equally important factor for maintaining the spinal cord window quality

when it comes to awake behavior. We found that high mobility of the spinal cord makes it more prone to injury. Even in the instantiation of miniscope imaging in freely behaving animals, short-term (∼2 to 3 min) restraint is necessary to attach the miniscope. We observed that even 2 to 3 min of restraint disturbs the quality of the spinal cord window in a poorly habituated mouse. Therefore, taking extra care in habituating to restraint and handling is essential. Alternatively, anesthetizing the animal allows simplified attachment of the miniscope. In our experience, attaching the miniscope under anesthesia works well for imaging unrestrained animals, but it cannot be easily applied to restraint experiments because animal awakening can cause sudden and forceful movements that damage the implant. However, every cycle of anesthetic use (e.g., isoflurane) can have an additive negative impact on the animal's health and ultimately reduces study duration.[20] We summarize the overarching timeline describing different major procedures and time intervals for each procedure as implemented for the final awake behavior experiments in this study in Fig. 5.

Optical access to the brain and spinal cord can be achieved via a single multiorgan surgery or two independent surgeries (Fig. 7). Some of the advantages for performing a single surgery are that it is possible to save experimental time because the animal and the surgical setup have to be prepared only once. Also the animal has to undergo the induction and recovery from anesthesia only once, as well as the postsurgical monitoring has to be performed only once. Furthermore, in the case of separate surgeries, there is a risk that the second surgery does not conclude successfully and hence the time spent after the first surgery will add to the experimental cost. However, in the case of a single surgery, it is possible to qualitatively assess the likelihood of successful experimental outcome by the end of a single surgical procedure.

However, big limitations of the simultaneous surgery are that it requires greater surgical skills and it is harder to include the local AAV injections as part of the simultaneous surgery. This has to do with the fact that AAV injections add significant amount of time that the animal has to spend under anesthesia and hence surgeon's technique needs to be optimized even more compared to simultaneous surgery without the injections. There are multiple alternatives that can be explored in the future to reduce the surgical duration and complexity. For example, two surgeons could rotate as part of the same procedure with each surgeon focusing only on one organ, as well as systemic AAVs, imaging windows coated with AAVs or transgenic animals can be used to achieve the genetic modifications required for the experiments without the need for injections as part of the same procedure. Finally, silicone implant windows could also be explored for local AAV delivery at later experimental stages.

Similar to the spinal cord implant design described in Ref. 69, our use of plastic for the implant chamber fabrication makes it more compatible with photoacoustic, ultrasound, and MRI imaging, as well as ultrasound stimulation and radiation therapy. We have not tested non-optical methods as part of this development process, and additional modifications might be needed to avoid artifacts. However, for nonminiscope imaging, set-screws are not necessary, and the plastics we tested can be threaded, decreasing component number. An important factor to consider when threading plastics is that these threads are more fragile than those in affixed nuts. In our experience, tapped threads reliably serve ∼2 to 3 screw–unscrew cycles. Replacing 000-120 screws with glue could be a solution but requires additional testing and we have not yet validated this approach.

5 Limitations

We have not applied the 3D-printed implant design described here to perform BL imaging. However, the stainless steel implants we used for BL imaging (Fig. 12) have the same optical properties as 3D-printed implants we used for FL imaging (Fig. 9). Both implant designs rely on identical glass window–tissue interfaces, and hence there is no reason to expect signal differences between them.

We were able to image calcium responses of individual neurons in the spinal cord for up to 37 days and dynamic "field" one-photon responses for up to 154 days. The dominant form of spinal cord implant failure was overgrowth of the window. As this report was in final stages of preparation, the first progress in mitigating the fibrosis in spinal cord optical windows was

described in Ref. 62 However, the issue of fibrosis has not been tracked quantitatively or mitigated within our work.

The experiments we present in Figs. 9(b) and 9(c) included simultaneous presence of eYFP (cre-dependent tagging of Trpv1 and CaV3.2) and GCaMP6f (CaMKIIα-dependent expression). Our laboratories have experience with calcium imaging in the presence of eYFP and we relied on extensive qualitative measures to ensure that the reported signals represent GCaMP6f rather than eYFP. However, we did not perform quantitative assessment of eYFP's influence on the quality of reported signals. Our logical not quantified expectation is that eYFP contributed higher background signal in our data and hence the recordings performed in the absence of eYFP [e.g., Fig. 9(a)] under the same other experimental conditions could potentially have higher signal-to-noise ratio.

Endogenous vascular responses we report in Fig. 10 require further in-depth characterization. The responses were repeatable across 30 trials, however, there was a high variability between different vascular segments and different animals (data not reported here; examples of the raw imaging data are included in the supplemental data repository accompanying this report). The exact mechanism underlying detected vascular responses is difficult to speculate about because we did genetically profile the spinal cord (e.g., for the presence of opsins). Another commonly considered confounding effect associated with optical stimulation is heating of the tissue. We cannot support the lack of thermal confounding effects with data because we did not spatially map the temperature inside the spinal cord and we are not aware of any studies that have characterized the thermal sensitivity specifically within the spinal cord. However, we use lower light intensities than typically is used for optogenetic experiments because the stimulation is turned off during the time periods when photomultiplier tube is collecting the photons (i.e., flyback stimulation summarized in Fig. 6). Furthermore, the endogenous opsins have been identified in the ventral horn of the spinal cord.[70] Even though there are no reports characterizing the expression of endogenous opsins in the dorsal spinal cord, there is ample evidence on endogenous opsins expressed in blood vessels in the heart,[71] lungs,[72] and brain.[66] Even though we have not characterized the blood vessel genetic composition in the spinal cord ourselves, it can be predicted that blood vessels in the spinal cord should not significantly differ from other internal organs.

Deeper assessment of animal immune responses and more prolonged chronic imaging in awake behaving animals across both brain and spinal cord, especially using microscopes optimized for BL, are key next steps.

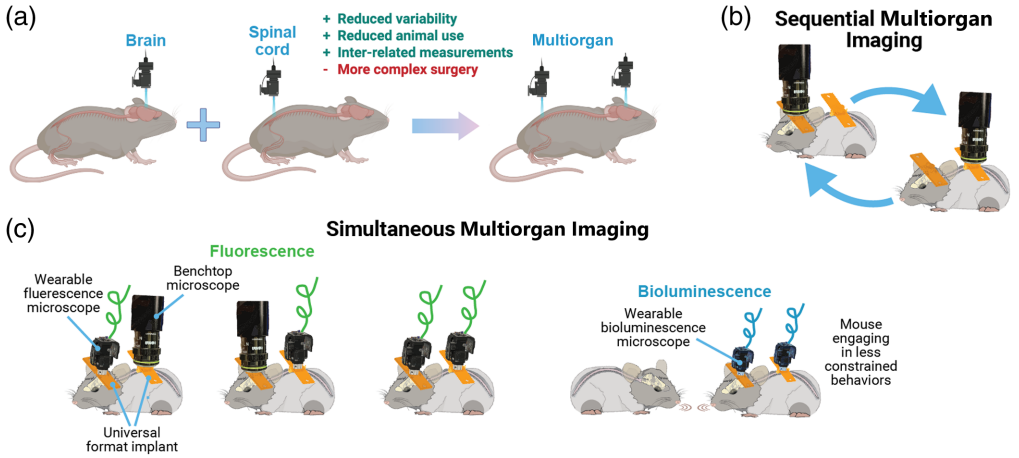

Fig. 13 Beyond brain-only imaging offers many opportunities for experimental designs and hardware combinations. (a) In this report, we demonstrate feasibility of gaining chronic optical access to the brain and spinal cord within the same animal. Universal format implants described as part of this report allow sequential (b) and simultaneous (c) imaging of the brain and spinal cord within the same animal using benchtop and wearable microscopes via FL or BL. Wearable microscopes for BL imaging, and hence the implants, can be designed smaller, allowing animals to engage in more natural behaviors. This figure was created partially with BioRender, Ref. 74.

6 Conclusion

Here we successfully developed and implemented a novel 3D printed brain–spinal cord implant, and advanced/refined surgical and sensory modulation procedures, to achieve simultaneous miniscope and two-photon imaging of the brain and spinal cord. This progress overcomes previous limitations [Fig. 13(a)], enabling detailed and prolonged observation of neural and vascular dynamics across multiple organs and expands the library of experimental designs accessible to scientists (Fig. 13). Our integration of BL imaging, with its novel indicators and modified miniscopes (BLmini), offers a potential alternative that can enhance multiorgan studies, offering simplified microscope design without confounding photoeffects. In essence, our contributions not only illuminate the path for next-generation neuroimaging but also inspire a reimagined approach to understanding the brain–spinal cord nexus, with far-reaching implications for science and medicine.

Disclosures

The authors declare no competing interests.

Code and Data Availability

The design files, codes, and data are available through the following DOI: https://doi.org/10.26300/2yeh-tr48.

Author contributions

Conceptualization: DC, DAB, CIM. Data curation: DC. Formal analysis: DC. Investigation: DC, ABA (performed surgery for the data in [Fig. 9(a)], NGF (performed surgery for the data in [Fig. 12(a)]. Methodology: DC. Visualization: DC. Writing – original draft preparation: DC. Writing – review: DC, CB, DAB, CIM. Writing – editing: DC, CIM. Resources: CB (provided resources for behavior experiments in animals with spinal implants), JM (provided resources for experiments on benchtop bioluminescence imaging), NS (provided molecules for bioluminescence imaging), MGR (provided resources for benchtop bioluminescence imaging), DAB (provided resources for spinal cord surgeries, miniscope imaging and data analysis), CIM (provided resources for all surgeries, all imaging modalities, behavior experiments and data analysis). Funding acquisition: NS (funding for bioluminescence work), CYS (funding for spinal surgery and sensory behavior development), DAB (funding for spinal surgery and sensory behavior development), CIM (funding for bioluminescence work). Supervision: DAB, CIM.

Acknowledgments

This work was supported by the National Science Foundation (NSF NeuroNex Grant No. 1707352) and the National Institute of Health (NIH NINDS Grant Nos. R01NS108414 and U01NS099709). Authors would like to thank Ute Hochgeschwender for providing AAV constructs, luciferin samples, and valuable discussions of experimental design of bioluminescence experiments. We would to thank Daniel Aharoni for support and valuable guidance in working with miniscopes, Chris Schaffer and his team for providing a tutorial on spinal cord surgeries, and helpful discussion on imaging and designs of the spinal window implants. We would like to thank Diane Lipscombe for providing Trpv1$^{ChR2eYFP+/-}$ and CaV3.2$^{ChR2eYFP+/-}$ mouse lines as well as for technical support with the bioluminescence benchtop testing and valuable discussions around the importance of UPRIM for studying sensory information processing. We would like to thank Thomas Kirkland and Joel Walker for providing fluorofurimazine samples for awake BL imaging. We would like to thank Adriana C. Salazar Coariti for valuable discussions around experimental design, optical engineering, and data visualization, Kimani C. Toussaint Jr. for valuable discussions around empirical testing of miniscopes, Jill Juneau for valuable discussions about electrical circuit design and troubleshooting of miniscopes, and Anusha Allawala for contributing to initial establishment of spinal cord surgeries and immunohistochemistry. We also would like to thank all members of the Bioluminescence Hub[73] for helpful discussions, especially Dr. Justine Allen for myriad levels of programmatic supporting and coordinating collaborative efforts, and Laurie Lynch for masterful animal colony and equipment management.

References

1. N. Rustamov et al., "Integration of bilateral nociceptive inputs tunes spinal and cerebral responses," *Sci. Rep.* **9**(1), 7143 (2019).
2. S. M. Carlton, "Nociceptive primary afferents: they have a mind of their own," *J. Physiol.* **592**(16), 3403–3411 (2014).
3. Y. Liu et al., "Touch and tactile neuropathic pain sensitivity are set by corticospinal projections," *Nature* **561**, 547–550 (2018).
4. R. W. Clarke and J. Harris, "The organization of motor responses to noxious stimuli," *Brain Res. Brain Res. Rev.* **46**(2), 163–172 (2004).
5. D. Blivis et al., "Identification of a novel spinal nociceptive-motor gate control for Aδ pain stimuli in rats," *eLife* **6**, e23584 (2017).
6. C. I. Moore and R. Cao, "The hemo-neural hypothesis: on the role of blood flow in information processing," *J. Neurophysiol.* **99**(5), 2035–2047 (2008).
7. L. Xia et al., "Dorsal-CA1 hippocampal neuronal ensembles encode nicotine-reward contextual associations," *Cell Rep.* **19**(10), 2143–2156 (2017).
8. K. J. Sekiguchi et al., "Imaging large-scale cellular activity in spinal cord of freely behaving mice," *Nat. Commun.* **7**, 11450 (2016).
9. A. A. Hamid, M. J. Frank, and C. I. Moore, "Wave-like dopamine dynamics as a mechanism for spatiotemporal credit assignment," *Cell* **184**(10), 2733–2749.e16 (2021).
10. M. J. Farrar et al., "Chronic in vivo imaging in the mouse spinal cord using an implanted chamber," *Nat. Methods* **9**(3), 297–302 (2012).
11. C. Chen et al., "Long-term imaging of dorsal root ganglia in awake behaving mice," *Nat. Commun.* **10**(1), 3087 (2019).
12. D. M. DuBreuil et al., "Heat but not mechanical hypersensitivity depends on voltage-gated CaV2.2 calcium channel activity in peripheral axon terminals innervating skin," *J. Neurosci.* **41**(36), 7546–7560 (2021).
13. T. A. Szabo-Pardi et al., "In vivo two-color 2-photon imaging of genetically-tagged reporter cells in the skin," *J. Vis. Exp.* (149), e59647 (2019).
14. T. Yn et al., "Imaging cellular signals in the heart in vivo: cardiac expression of the high-signal Ca^{2+} indicator GCaMP2," *Proc. Natl. Acad. Sci. U. S. A.* **103**(12), 4753–4758 (2006).
15. R. Zayats, J. E. Uzonna, and T. T. Murooka, "Visualizing the in vivo dynamics of anti-leishmania immunity: discoveries and challenges," *Front. Immunol.* **12**, 671582 (2021).
16. M. Desai et al., "Mapping brain networks in awake mice using combined optical neural control and fMRI," *J. Neurophysiol.* **105**(3), 1393–1405 (2011).
17. I. Kahn et al., "Optogenetic drive of neocortical pyramidal neurons generates fMRI signals that are correlated with spiking activity," *Brain Res.* **1511**, 33–45 (2013).
18. S. Vahdat et al., "Resting-state brain and spinal cord networks in humans are functionally integrated," *PLoS Biology* **18**(7), e3000789 (2020).
19. L. K. Diaz et al., "Increasing cumulative exposure to volatile anesthetic agents is associated with poorer neurodevelopmental outcomes in children with hypoplastic left heart syndrome," *J. Thorac. Cardiovasc. Surg.* **152**(2), 482–489 (2016).
20. N. M. Bajwa et al., "Repeated isoflurane in adult male mice leads to acute and persistent motor decrements with long-term modifications in corpus callosum microstructural integrity," *J. Neurosci. Res.* **97**(3), 332–345 (2019).
21. S. Kohtala et al., "Brief isoflurane anesthesia produces prominent phosphoproteomic changes in the adult mouse hippocampus," *ACS Chem. Neurosci.* **7**(6), 749–756 (2016).
22. J. Liu et al., "Effects of different concentration and duration time of isoflurane on acute and long-term neurocognitve function of young adult C57BL/6 mouse," *Int. J. Clin. Exp. Pathol.* **7**(9), 5828–5836 (2014).
23. L. Peng et al., "Histone deacetylase 2-mediated epigenetic regulation is involved in the early isoflurane exposure-related increase in susceptibility to anxiety-like behaviour evoked by chronic variable stress in mice," *Neurochem. Res.* **46**(9), 2333–2347 (2021).
24. C. Constantinides, R. Mean, and B. J. Janssen, "Effects of isoflurane anesthesia on the cardiovascular function of the C57BL/6 mouse," *ILAR J.* **52**(3), e21–31 (2011).
25. P. M. Cornett, J. A. Matta, and G. P. Ahern, "General anesthetics sensitize the capsaicin receptor transient receptor potential V1," *Mol. Pharmacol.* **74**(5), 1261–1268 (2008).
26. P. Orestes et al., "Mechanisms and functional significance of inhibition of neuronal T-type calcium channels by isoflurane," *Mol. Pharmacol.* **75**(3), 542–554 (2009).
27. Q. Li et al., "Effects of early exposure to isoflurane on susceptibility to chronic pain are mediated by increased neural activity due to actions of the mammalian target of the Rapamycin pathway," *Int. J. Mol. Sci.* **24**(18), 13760 (2023).
28. J. Voigts et al., "The flexDrive: an ultra-light implant for optical control and highly parallel chronic recording of neuronal ensembles in freely moving mice," *Front. Syst. Neurosci.* **7**, 8 (2013).

29. S. P. Peron et al., "A cellular resolution map of barrel cortex activity during tactile behavior," *Neuron* **86**(3), 783–799 (2015).
30. Z. Wei et al., "A comparison of neuronal population dynamics measured with calcium imaging and electrophysiology," *PLoS Comput. Biol.* **16**(9), e1008198 (2020).
31. W. Zong et al., "Large-scale two-photon calcium imaging in freely moving mice," *Cell* **185**(7), 1240–1256.e30 (2022).
32. I. Costantini et al., "Autofluorescence enhancement for label-free imaging of myelinated fibers in mammalian brains," *Sci. Rep.* **11**(1), 8038 (2021).
33. H. Yukawa et al., "Influence of autofluorescence derived from living body on in vivo fluorescence imaging using quantum dots," *Cell Med.* **7**(2), 75–82 (2014).
34. A. Ayaz et al., "Layer-specific integration of locomotion and sensory information in mouse barrel cortex," *Nat. Commun.* **10**(1), 2585 (2019).
35. N. A. Nelson et al., "Imaging spinal cord activity in behaving animals," *Exp. Neurol.* **320**, 112974 (2019).
36. A. Fukui et al., "Layer-specific sensory processing impairment in the primary somatosensory cortex after motor cortex infarction," *Sci. Rep.* **10**(1), 3771 (2020).
37. J. Borowska et al., "Functional subpopulations of V3 interneurons in the mature mouse spinal cord," *J. Neurosci.* **33**(47), 18553–18565 (2013).
38. A. Raghuram et al., "Determining the depth limit of bioluminescent sources in scattering media," p. 2020.04.21.044982, bioRxiv (2020).
39. S. Ramón y Cajal, *Comparative Study of the Sensory Areas of the Human Cortex*, Clark University (1899).
40. S. Ramón y Cajal, "Les nouvelles idées sur la structure du système nerveux : chez l'homme et chez les vertébrés," édition française revue et augmentée par l'auteur ; traduite de l'espagnol par L. Azoulay; preface de M. Mathias-Duval (1894).
41. Y. Hontani, F. Xia, and C. Xu, "Multicolor three-photon fluorescence imaging with single-wavelength excitation deep in mouse brain," *Sci. Adv.* **7**(12), eabf3531 (2021).
42. J. Icha et al., "Phototoxicity in live fluorescence microscopy, and how to avoid it," *Bioessays* **39**(8), 1700003 (2017).
43. B. I. Pinto, C. A. Z. Bassetto, and F. Bezanilla, "Optocapacitance: physical basis and its application," *Biophys. Rev.* **14**(2), 569–577 (2022).
44. M. R. Hamblin, "Shining light on the head: photobiomodulation for brain disorders," *BBA Clin.* **6**, 113–124 (2016).
45. D. Aharoni and T. M. Hoogland, "Circuit investigations with open-source miniaturized microscopes: past, present and future," *Front. Cell. Neurosci.* **13**, 141 (2019).
46. D. Aharoni et al., "All the light that we can see: a new era in miniaturized microscopy," *Nat. Methods* **16**(1), 11–13 (2019).
47. C. Guo et al., "Miniscope-LFOV: a large-field-of-view, single-cell-resolution, miniature microscope for wired and wire-free imaging of neural dynamics in freely behaving animals," *Sci. Adv.* **9**(16), eadg3918 (2023).
48. J. Juneau et al., "MiniFAST: a sensitive and fast miniaturized microscope for in vivo neural recording," p. 2020.11.03.367466, bioRxiv (2020).
49. O. Skocek et al., "High-speed volumetric imaging of neuronal activity in freely moving rodents," *Nat. Methods* **15**(6), 429–432 (2018).
50. A. de Groot et al., "NINscope, a versatile miniscope for multi-region circuit investigations," *eLife* **9**, e49987 (2020).
51. Y. Qian et al., "A bioluminescent Ca^{2+} indicator based on a topological variant of GCaMP6s," *Chembiochem* **20**(4), 516–520 (2019).
52. N. Mertes et al., "Fluorescent and bioluminescent calcium indicators with tuneable colors and affinities," *J. Am. Chem. Soc.* **144**(15), 6928–6935 (2022).
53. X. Tian et al., "A luciferase prosubstrate and a red bioluminescent calcium indicator for imaging neuronal activity in mice," *Nat. Commun.* **13**(1), 3967 (2022).
54. M. N. Hossain et al., "Bioluminescent low-affinity Ca^{2+} indicator for ER with multicolor calcium imaging in single living cells," *ACS Chem. Biol.* **13**(7), 1862–1871 (2018).
55. G. G. Lambert et al., "CaBLAM! a high-contrast bioluminescent Ca^{2+} indicator derived from an engineered *Oplophorus gracilirostris* luciferase," bioRxiv, 2023.06.25.546478 (2023).
56. 3D-printing service provider, 3D Systems, Inc., www.3dsystems.com (accessed February 2022).
57. Machining and online store of miniscope parts, miniscopeparts.com (accessed February 2024).
58. M. Gomez-Ramirez et al., "The BioLuminescent-OptoGenetic in vivo response to coelenterazine is proportional, sensitive, and specific in neocortex," *J. Neurosci. Res.* **98**(3), 471–480 (2020).
59. D. Celinskis et al., "Miniaturized devices for bioluminescence imaging in freely behaving animals," in *Annu. Int. Conf. IEEE Eng. Med. Biol. Soc.*, pp. 4385–4389 (2020).

60. M. Harrison et al., "Vertebral landmarks for the identification of spinal cord segments in the mouse," *Neuroimage* **68**, 22–29 (2013).
61. J. Voigts, C. A. Deister, and C. I. Moore, "Layer 6 ensembles can selectively regulate the behavioral impact and layer-specific representation of sensory deviants," *eLife* **9**, e48957 (2020).
62. B. Ahanonu et al., "Long-term optical imaging of the spinal cord in awake, behaving animals," bioRxiv, 2023.05.22.541477 (2023).
63. M. J. Farrar et al., "Characterization of blood flow in the mouse dorsal spinal venous system before and after dorsal spinal vein occlusion," *J. Cereb. Blood Flow Metab.* **35**(4), 667–675 (2015).
64. Y.-T. Cheng, K. M. Lett, and C. B. Schaffer, "Surgical preparations, labeling strategies, and optical techniques for cell-resolved, in vivo imaging in the mouse spinal cord," *Exp. Neurol.* **318**, 192–204 (2019).
65. R. F. Furchgott, S. J. Ehrreich, and E. Greenblatt, "The photoactivated relaxation of smooth muscle of rabbit aorta," *J. Gen. Physiol.* **44**(3), 499–519 (1961).
66. R. L. Rungta et al., "Light controls cerebral blood flow in naive animals," *Nat. Commun.* **8**(1), 14191 (2017).
67. C. J. Black et al., "Automated and rapid self-report of nociception in transgenic mice," *Sci. Rep.* **10**(1), 13215 (2020).
68. W. Wu et al., "Publisher correction: long-term in vivo imaging of mouse spinal cord through an optically cleared intervertebral window," *Nat. Commun.* **13**(1), 3930 (2022).
69. N. Yang et al., "A hybrid titanium-softmaterial, high-strength, transparent cranial window for transcranial injection and neuroimaging," *Biosensors* **12**(2), 129 (2022).
70. S. Blackshaw and S. H. Snyder, "Encephalopsin: a novel mammalian extraretinal opsin discretely localized in the brain," *J. Neurosci.* **19**(10), 3681–3690 (1999).
71. G. Sikka et al., "Melanopsin mediates light-dependent relaxation in blood vessels," *Proc. Natl. Acad. Sci. U. S. A.* **111**(50), 17977–17982 (2014).
72. S. Barreto Ortiz et al., "Opsin 3 and 4 mediate light-induced pulmonary vasorelaxation that is potentiated by G protein-coupled receptor kinase 2 inhibition," *Am. J. Physiol.-Lung Cell. Mol. Physiol.* **314**(1), L93–L106 (2018).
73. The Bioluminescence Hub, www.bioluminescencehub.org (accessed February 2024).
74. BioRender – a platform for creating scientific figures, www.biorender.com (accessed March 2024).

Dmitrijs Celinskis leverages his Brown University PhD in Biomedical Engineering and Medical Physics background to drive innovation in brain-computer interfaces and medical device development. His clinical research expertise, paired with hands-on neurotechnology experience (benchtop and *in vivo* testing, neuromodulation, scientific computing), fuels the creation of impactful solutions. Recognized for his translational work, Dmitrijs seeks to bridge groundbreaking technologies with clinical needs for transformative patient care.

Christopher J. Black is a postdoctoral fellow in Dr. Robert Brownstone's Laboratory at University College London, United Kingdom. He received his PhD in biomedical engineering from Brown University in 2022, where he examined neural correlates of somatosensation. His current research focuses on applying engineering and computational approaches to better understand the functional role of higher-order neural circuits in regulating sensorimotor function during ALS.

Jeremy Murphy is a PhD scientist at the Bioluminescent Hub.[73] He tests bioluminescent molecules developed by the Hub for reading and writing brain activity in mice. He also uses these molecular tools to answer questions about the basic circuitry of the mammalian brain. Testing and employing these bioluminescent tools usually involves imaging bioluminescence with a very sensitive camera while also recording the electrical activity of neurons in the brain using silicon-based microelectrodes.

Nina G. Friedman is a graduate student investigating the basic computations of perception using two-photon holography in mouse neocortex. She works in Dr. Mark Histed's Group at the National Institute of Mental Health (NIMH). Before coming to the University of Maryland, she studied neuroscience at Colorado College for her bachelor's degree, later joining Dr. Chris Moore's Lab at Brown University as a research assistant. At Brown, she worked with the Bioluminescence Hub,[73] developing tools that use bioluminescent light to drive and report cell activity.

Nathan C. Shaner is an associate professor in the Department of Neurosciences at UCSD. In 2002, he joined Dr. Roger Tsien's Lab as a graduate student in the Biomedical Sciences

Graduate Program at UCSD and completed his PhD training in 2006. He then moved on to two postdoctoral research positions, the first at Salk Institute with Dr. Joanne Chory and the second at Monterey Bay Aquarium Research Institute with Dr. Steven Haddock, where he studied transcriptomics of bioluminescent organisms. He moved back to San Diego as a founding investigator at the Scintillon Institute in 2012. In 2018, he moved to his current faculty position at UCSD.

Carl Y. Saab is a neuroscientist with postdoctoral training from Yale followed by 16 years as faculty at Brown. Currently, he is a professor of biomedical engineering at Cleveland Clinic and Case Western Reserve University and a founder and a director of the Cleveland Clinic Consortium for Pain. His lab studies neural circuits of mental health and neurological disorders in the brain. His research led to the discovery of neural signatures that can be used to measure pain and analgesic efficacy.

David A. Borton is an associate professor of engineering and brain science at Brown University, an associate professor of neurosurgery at Rhode Island Hospital, and a biomedical engineer at the Providence VA Medical Center of Center for Neurorestoration and Neurotechnology. He received his BS degree in biomedical engineering from Washington University in St. Louis in 2006, his PhD in bioengineering from Brown University in 2012, and performed a Marie Curie postdoctoral fellowship at the Ecole Polytechnique Fèdèrale de Lausanne from 2012 to 2014. He leads an interdisciplinary team of researchers focused on the design, development, and deployment of innovative neural recording and stimulation technologies.

Christopher I. Moore is a professor of neuroscience at Brown University and associate director of the Robert J. and Nancy D. Carney Institute for Brain Science. He earned his PhD from MIT and held a postdoctoral fellowship at Harvard Medical School. His notable contributions include work on thalamic reticular nucleus and its role in neocortical spindles, highlighted in *Nature Neuroscience*. He studies neurovascular dynamics and their role in information processing, and develops new technologies to test how phenomena, such as ongoing brain activity patterns, impact perception.

Biographies of the other authors are not available.